Conceptual Design of High Resolution and Quantitative SPECT System for Imaging a Selected Small ROI of human brain

Tsutomu Zeniya, Yoshiyuki Hirano, Tomonori Sakimoto, Kenji Ishida, Hiroshi Watabe, *Member, IEEE*, Noboru Teramoto, Hiroyuki Kudo, *Member, IEEE*, Kotaro Minato, *Member, IEEE*, Jun Hatazawa, and Hidehiro Iida, *Member, IEEE*

Abstract– **We designed a concept of high resolution and quantitative SPECT for imaging a selected small region-of-interest (ROI) of human brain. This system is aimed at achieving high resolution less than 1 mm and being applied for imaging neurons and evaluating drug delivery system. Pinhole or cone-beam collimators are useful for high-resolution imaging of small ROI. However, when the ROI is smaller than the object, the projection data are truncated by radioisotope outside ROI. In the reconstructed image, the truncation causes the artifact and the overestimation of voxel value, which deceases quantitative accuracy of physiological functions. We are introducing the new truncation compensated 3D-OSEM (TC-3DOSEM) reconstruction method. The truncated data can be successfully reconstructed within ROI by fulfilling the condition that ROI contains a priori knowledge. In addition to small field-of-view (FOV) detector, we are introducing the parallel-hole collimator attached large FOV detector covering the entire brain, to acquire the non-truncated data and provide the priori knowledge in small ROI, even if the resolution of the detector is low. For imaging with high resolution, we are using $LaBr_3(Ce)$ scintilator with optically coupled to position-sensitive photomultiplier tube (H8500, Hamamatsu, Japan) as the detector. And also, for proof of our concept, we performed preliminary experiment using pinhole SPECT and brain phantom. The reconstruction ROI contained the region outside the brain, that is, zero count as the priori knowledge. The truncated data were reconstructed by TC-3DOSEM. The reconstructed image without artifact and overestimation was obtained with high resolution. This preliminary experiment suggested feasibility of high resolution and quantitative SPECT for imaging a selected small ROI of human brain.**

Manuscript received November 13, 2009. This work was supported in part by the Grant-in-Aid for Scientific Research (C) (20500435) of the Ministry of Education, Culture, Sports and Technology (MEXT), Japan, the Grant for Translational Research from the Ministry of Health, Labour and Welfare (MHLW), Japan, Newly Adopted Projects of Regional R&D Programs for FY2008 from Kansai Bureau of Economy, Trade and Industry, Japan.

T. Zeniya, Y. Hirano, K. Ishida, H. Watabe, N. Teramoto and H. Iida are with the Department of Investigative Radiology, Advanced Medical Engineering Center, National Cardiovascular Center Research Institute, 5-7-1 Fujishirodai, Suita, Osaka 565-8565 Japan (e-mail: zeniya @ri.ncvc.go.jp).

T. Sakimoto and K. Minato with the Graduate School of Information Science, Nara Institute of Science and Technology, Japan.

H. Kudo is with the Department of Computer Science, Graduate School of Systems and Information Engineering, University of Tsukuba, Japan.

J. Hatazawa is with the Department of Nuclear Medicine and Tracer Kinetics, Osaka University Graduate School of Medicine, Japan.

I. Introduction

We designed a concept of high resolution and quantitative SPECT for imaging a selected small region-of-interest (ROI) of human brain. This system is aimed at achieving high resolution less than 1 mm and being applied for imaging neurons and evaluating drug delivery system. Also, for proof of our concept, we carried out preliminary experiment using pinhole SPECT and brain phantom.

II. Conceptual Design

Pinhole or cone-beam collimators are useful for high-resolution imaging of small ROI. However, as shown in Fig. 1, when the reconstruction ROI is smaller than the object like human brain, the projection data are truncated by radioisotope outside ROI. Because of this truncation, the voxel value of the reconstructed image is overestimated. This hampers quantitative assessment of physiological functions.

Recently, Kudo et al proposed reconstruction theory to solve the interior problem in computed tomography (CT) [1]. We are applying it for pinhole and cone-beam SPECT. Let's explain how to realize with Fig. 2. According to Kudo's theory, the truncated data can be successfully reconstructed within ROI by fulfilling the condition that ROI contains a priori knowledge. In addition to small field-of-view (FOV) detector for imaging with high resolution, we are introducing the parallel-hole collimator attached large FOV detector covering the entire brain to acquire the non-truncated data, even if the resolution of the detector is low. As another condition, the reconstruction matrix must be larger than the object.

Figure 3 is a conceptual illustration of high resolution and quantitative SPECT system for imaging a selected small ROI of human brain. This system has two types of detectors. One is pinhole or cone-beam collimator attached $LaBr_3(Ce)$ scintillator with high intrinsic spatial resolution of approximately 1 mm [2] for imaging a selected small ROI with high resolution. The other is parallel-hole collimator attached NaI(Tl) scintillator with active area of 250 mm × 150 mm for acquiring the non-truncated data. Position-sensitive photomultiplier tubes (H8500, Hamamatsu, Japan) are optically coupled to both scintilators.

9781-4244-3962-1/09/$25.00 ©2009 IEEE

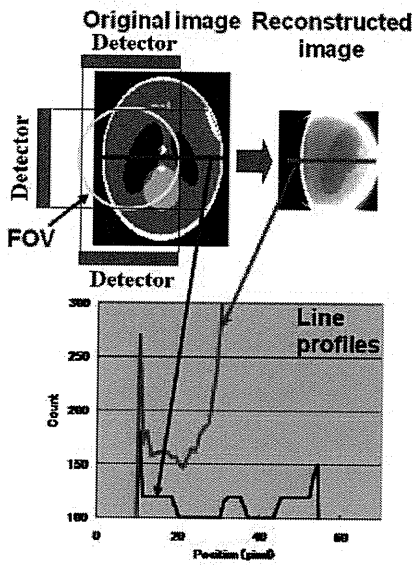

Fig. 1. The artifact and overestimation on the reconstructed image due to truncation.

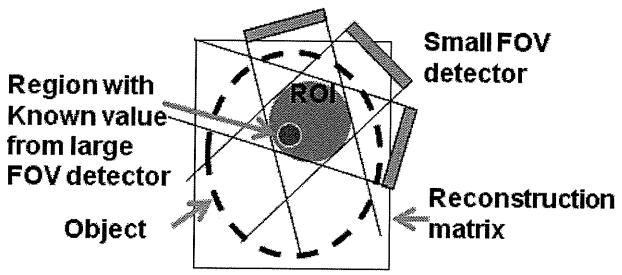

Fig. 2. Schematic diagram showing the solution of the interior problem.

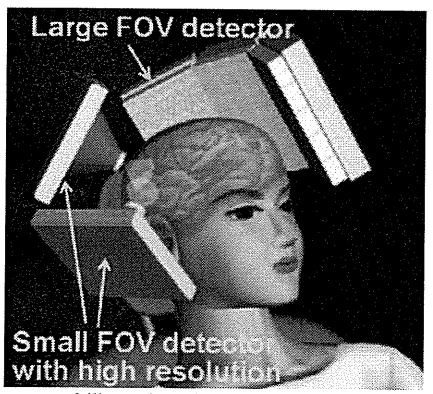

Fig. 3. Conceptual illustration of high resolution and quantitative SPECT system for imaging a selected small ROI of human brain.

III. Preliminary Experiment

For proof of our concept, we performed preliminary experiment using pinhole SPECT and Hoffman brain phantom [3]. The reconstruction ROI contained the region outside the brain, that is, almost zero count as the priori knowledge [4]. The truncated data were reconstructed by truncation compensated 3D-OSEM (TC-3DOSEM) reconstruction method for pinhole SPECT [5].

Figure 4 shows the experimental setup. We scanned a part of Hoffman brain phantom using the rotating stage and 1-mm pinhole collimator fitted to clinical SPECT gamma camera (GCA7200A, Toshiba, Japan). As for the scan parameters, the phantom was filled with Tc-99m of 1,480 MBq and scanned for 2 hours, the radius of rotation was 95mm, the imaging FOV was 95 mm, and the rotation angle was 180 degrees. This radius of rotation is that collimator doesn't hit again the phantom in case of circular orbit and 180 degrees rotation. And also, we scanned same phantom using parallel collimator to compare in terms of spatial resolution.

Fig. 4. Experimental setup for scanning Hoffman brain phantom by pinhole SPECT.

Figure 5 shows results of human brain phantom study. In case of clinical SPECT with parallel collimator, the resolution of the reconstructed image was low. In case of pinhole collimator and conventional 3DOSEM, the resolution was high, but the artifact appeared at the edge of ROI and the voxel counts were overestimated. On the other hand, combination of pinhole collimator and TC-3DOSEM provide high resolution image and eliminated the artifact and the overestimation. In this experimental geometry using pinhole collimator, theoretical resolution was approximately 2 mm.

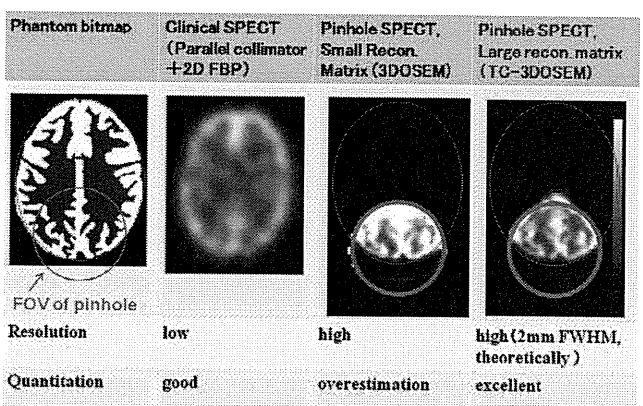

Fig. 5. Comparison of the reconstructed image from preliminary experiment using brain phantom.

IV. Conclusion

We have designed the concept of high resolution and quantitative SPECT for imaging a selected small ROI of human brain. And also, the preliminary experiment suggested

feasibility of high resolution and quantitative SPECT for human brain.

REFERENCES

[1] H. Kudo, M. Courdurier, F. Noo, and M. Defrise, "Tiny a prior knowledge solves the interior problem in computed tomography," *Phys. Med. Biol.*, vol. 53, no. 9, pp. 2207-2231, 2008.

[2] R. Pani, R. Pellegrini, M. N. Cinti, P. Bennati, M. Betti *et al.*, "$LaBr_3$:Ce crystal: The latest advance for scintillation cameras," *Nucl Instrum Meth A.*, vol. 572, pp. 268-269, 2007.

[3] E. J. Hoffman, P. D. Cutler, W. M. Digby, and J. C. Mazziotta, "3D phantom to simulate cerebral blood flow and metabolic images for PET," *IEEE Trans. Nucl. Sci.*, vol. 37, pp. 616-620, 1990.

[4] M. Defrise, F. Noo, R. Clackdoyle, and H. Kudo, "Truncated Hilbert transform and image reconstruction from limited tomographic data," *Inverse Problems*, vol. 22, pp. 1037-1053, 2006.

[5] T. Zeniya, H. Watabe, A. Sohlberg, T. Inomata, H. Kudo, et al., "3D-OSEM reconstruction from truncated data in pinhole SPECT," *2007 IEEE Nuclear Science Symposium Conference Record*, vol. 6, pp. 4205-4207, 2007.

Interior SPECT Reconstruction Problem with Tiny *a proiri* Knowledge – An Application for High Resolution Pinhole Brain Imaging

Qiu Huang, Tsutomu Zeniya, Hiroyuki Kudo, Hidehiro Iida, and Grant T. Gullberg

Abstract— **The quantitation of cerebral blood flow (CBF) and cerebral vascular reactivity (CVR) are valuable in diagnosing brain ischemia, and the quantitation of benzodiazepine receptor density is important in evaluating neuronal damage due to ischemic effects. To better evaluate cerebral autoregulation, a high resolution brain single photon emission computed tomography (SPECT) imager is being built that provides an image of the entire brain for support information in the reconstruction of the interior problem from small field-of-view, truncated projections for high resolution ROI imaging.**

Kudo *et al.* presented a unique and stable solution to the interior problem in computed tomography (CT) given tiny *a proiri* knowledge of the object. In this work we advance their result to the interior reconstruction problem in SPECT where a uniform attenuation map is assumed in brain imaging.

In the theory, differentiation followed by backprojection (DBP) of truncated SPECT data is shown to obtain the truncated weighted Hilbert transform. Then with *a proiri* information on a small part of the region-of-interest (ROI), the other part of the ROI is shown to be available using the projection onto convex sets (PCOS) method. Simulations show that the algorithm provides quantitative results for the reconstruction of the fan-beam tomographic data. Iterative reconstruction of the pinhole data is under investigation to verify the accuracy of the central slice and to provide reasonable results for regions off the central slice.

Index Terms—**interior problem, SPECT, uniform attenuation, brain imaging.**

I. Introduction

The Department of Investigative Radiology at the National Cardiovascular Center Research Institute in Osaka, Japan is designing a high resolution single photon emission computed tomography (SPECT) imager for obtaining high resolution brain scans for various imaging diagnostic applications. The camera consists of one large field of view detector imaging the whole brain and multiple smaller field of view high resolution detectors imaging small regions of the brain (see Fig. 1). The large field of view detector provides images without truncation that localize areas of particular diagnostic interest and provide support information for the reconstruction of high resolution regions of interest (ROIs) from high resolution truncated projections obtained with the small field of view detectors. The work presented in this paper develops an algorithm that accurately reconstructs uniformly attenuated truncated projections, which is an extension of the interior reconstruction problem for the reconstruction of non attenuated truncated projections.

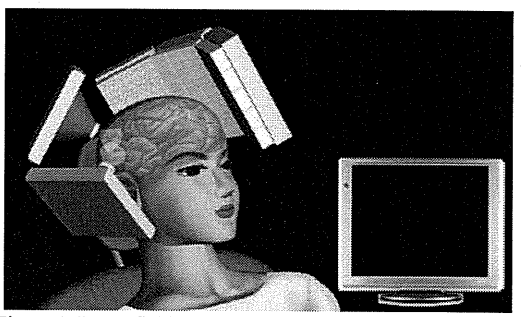

Figure 1. Large field of view detector for imaging whole brain and smaller field of view detectors for imaging ROIs.

The Department of Investigative Radiology has been involved in a large-scale multicenter clinical study aimed at evaluating validity and impact of a quantitative SPECT reconstruction package (QSPECT) [1] for multicenter clinical studies. The quantitative SPECT reconstruction package provides quantitative functional parametric images which are consistent among different setup of equipments and institutions. This allows the use of SPECT in a large scale clinical evaluation for diagnosing brain autoregulatory abnormalities. (A review of noninvasive diagnostic tests to assess cerebral autoregulation can be found in [2].) Dynamic SPECT scans are used to quantify cerebral blood flow (CBF) and cerebral vascular reactivity (CVR) in a single session using a split dose administration of ^{123}I iodo-amphetamine (IMP); one at rest and one during Diamox challenge [3]. Clinical data using QSPECT demonstrated that CBF at rest and during Diamox was reproducible among institutions.

This work was supported in part by the National Institutes of Health under Grant R01 EB00121, and in part by the Director, Office of Science, Office of Biological and Environmental Research, Medical Sciences Division of the U.S. Department of Energy under Contract DE-AC02-05CH11231.

Qiu Huang is with Lawrence Berkeley National Laboratory, One Cyclotron Road, MS 55R0121, Berkeley, CA 94720-8119. (phone: 510-495-2714; fax: 510-486-4768; e-mail: qhuang@lbl.gov).

Tsutomu Zeniya is with the National Cardiovascular Center Research Institute, Suita, Osaka, Japan (e-mail: zeniya @ri.ncvc.go.jp).

Hiroyuki Kudo is with University of Tsukuba, Tsukuba, Japan (e-mail: kudo@*is*.tsukuba.ac.jp).

Hidehiro Iida is with the National Cardiovascular Center Research Institute, Suita, Osaka, Japan (e-mail: iida@ri.ncvc.go.jp).

Grant T. Gullberg is with Lawrence Berkeley National Laboratory, One Cyclotron Road, MS 55R0121, Berkeley, CA 94720-8119. (e-mail: gtgullberg@lbl.gov).

Another important part of the multi-center trial is to evaluate neuronal damage due to ischemia and to provide prognostic value for surgical outcomes. Damage of benzodiazepine receptors has been found in cases of patients with severe brain ischemia [4]. Also, alterations of central benzodiazepine receptors have been described in several neuropsychiatric conditions, including epilepsy, Alzheimer's disease, Huntington's chorea and schizophrenia. Carbon-11-flumazenil, a benzodiazepine antagonist, has been used as a PET radiotracer for visualization and quantification of benzodiazepine receptors in humans. Recently, an iodinated analog of flumazenil, iomazenil has been introduced as a SPECT radiotracer. SPECT imaging of iodine-123-iomazenil (Iomazenil) binding to benzodiazepine receptors in the brain is being used to evaluate neuronal damage caused by ischemia [4] and the prognosis prior to carotid endoarterectomy [5]. Kinetic model-based methods have been developed for SPECT to quantitatively measure ^{123}I-iomazenil binding to benzodiazepine receptors in the human brain [6].

The Department of Investigative Radiology is developing a camera that will perform high resolution imaging of local ROIs in the brain to better address these imaging applications. Imaging with a high resolution small field of view camera provides truncated projections. The reconstruction of these projections involves determining the solution to the interior problem in local tomography. The interior problem in medical imaging refers to the situation where the region-of-interest (ROI) is totally contained within the object. For instance, in SPECT, the interior problem happens when the projections passing through the region outside the ROI are truncated due to a small field-of-view detector or a short detector-to-object distance in the case of converging collimation. The interior problem has been studied for some time [7]. Recently, Kudo *et al.* [8] proved that the solution is unique and stable in computed tomography (CT) if a small region in the ROI is known *a proiri*. In this paper this result is extended to the SPECT interior reconstruction problem.

Both in the work of Kudo *et al.* and in the work presented in this paper, the theory for the solution to the interior problem is based on the differentiation backprojection (DBP) method. The concept of DBP was first developed in parallel beam [9] and cone-beam [10] geometry in CT. The non interior truncation problem was solved for CT in [11], [12], [13], [14], [15]. Similar works in SPECT can be found in [16], [17], [18], [19], [20], where uniform attenuation was assumed. In SPECT the assumption of uniform attenuation is reasonable for some applications such as in brain imaging [21]. The result of the work in this paper shows that, with *a proiri* information of the ROI, the brain image can be reconstructed even when the imaging geometry forms an interior problem. It is expected that this result is useful in the reconstruction of pinhole data, where a pinhole collimator is attached to the small field-of-view cameras for imaging the brain. The pinhole collimator provides a small field-of-view (FOV) with high sensitivity and high resolution when located close to the object.

The paper is organized as follows: Section II shows that the differentiated backprojection (DBP) of fan-beam data is related to the distribution of the radioactive tracer in SPECT through a truncated weighted Hilbert transform. Then a unique inversion is shown to exist for the truncated weighted Hilbert transform given a small region of ROI is known *a proiri*. The results of numerical simulations are presented in Section III where the theory is shown to give a measure of confidence for the quantitative accuracy of the fan-beam reconstruction problem and the conclusion is given in Section IV.

II. Method

The method in this work is illustrated by showing that the differentiated backprojection (DBP) of fan-beam data is related to the distribution of the radioactive tracer in SPECT through a truncated weighted Hilbert transform and the truncated weighted Hilbert transform can be inverted given some prior information.

A. DBP operation for fan-beam data

For a transaxial slice, let $f(x,y)$ represent the distribution of the radiopharmaceutical in body tissues, which is assumed to be a smooth and compactly supported function of R^2. The SPECT image reconstruction estimates $f(x,y)$ from the detected photon counts. We denote $\vec{r}=(x,y)$ and $D=\{(x,y)\in R^2:\ x^2+y^2\le 1\}$. We assume $f(x,y)\equiv 0$ outside of D and the attenuation μ of the body tissues is uniform inside D. A typical fan-beam data acquisition geometry with a circular focal-point trajectory is shown in Fig. 2, where each projection ray is represented by (β,σ). One particular projection ray is shown emanating from the focal point S for the angle β with the ray angle σ.

In this paper, the fan-beam uniformly attenuated projection of the function $f(x,y)$ is defined as

$$[D_\mu f](\beta,\sigma)=\int_0^\infty f(S+\tau\vec{\alpha}(\beta,\sigma))e^{\mu\tau}d\tau\,, \qquad (1)$$

where $D_\mu f$ is the projection operator for the uniformly attenuated fan-beam projection data, $\sigma\in[-\sigma_m,\sigma_m]$, and $\vec{\alpha}(\beta,\sigma)$ is a unit vector in R^2 representing the direction from the focal point to the collimation hole, as shown in Fig. 2. Here, $\sigma_m\in(0,\pi/2)$ denotes the maximum angle subtended by the fan-beam. Let R be the radius of the circular focal point trajectory. We can modify the fan-beam data to obtain:

$$g(\beta,\sigma)=e^{-\mu R\cos\sigma}[D_\mu f](\beta,\sigma)\,. \qquad (2)$$

Define

$$s=R\sin\sigma,\quad \theta=\sigma+\beta$$

$$\hat{\sigma}(r,\varphi,\theta)=\arcsin\frac{\vec{r}\cdot\vec{\theta}}{R}=\arcsin\frac{r\cos(\theta-\varphi)}{R}\,.$$

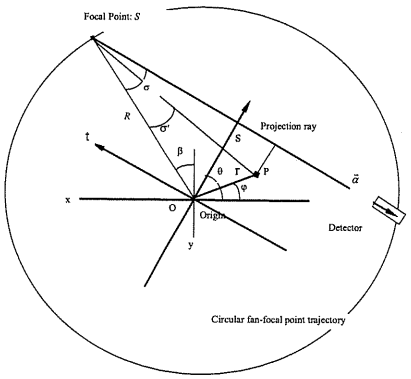

Figure 2. A typical fan-beam acquisition geometry.

We denote $\vec{\theta} = (\cos\theta, \sin\theta)$ and $\vec{\theta}^{\perp} = (-\sin\theta, \cos\theta)$ and construct an image:

$$\hat{f}(x,y) = -\frac{1}{2}\int_{-\pi/2}^{\pi/2} \frac{e^{\mu\vec{r}\cdot\vec{\theta}^{\perp}}[(\frac{\partial}{\partial\sigma}-\frac{\partial}{\partial\beta})g](\theta-\hat{\sigma}(r,\varphi,\theta),\hat{\sigma}(r,\varphi,\theta))}{R\cos\hat{\sigma}(r,\varphi,\theta)}d\theta. \quad (3)$$

This image was proved to be related to the original distribution of radiopharmaceutical as [17]:

$$\hat{f}(x,y) = \int_{-\infty}^{\infty} \frac{\cosh(\mu\tau)f(x-\tau,y)}{\pi\tau}d\tau. \quad (4)$$

Equation (3) involves the operations of derivative and backprojection for the modified attenuated projection in fan-beam geometry and can be readily obtained from fan-beam measurements. Equation (4) shows that the image $\hat{f}(x,y)$ is an image obtained by convolving the true image with a one-dimensional (1D) kernel $\cosh(\mu t)/(\pi t)$ multiplied by some factor, thus the image reconstruction is accomplished by inverting the convolution corresponding to a truncated weighted Hilbert transform.

B. Inversion of Truncated Hilbert Transform

Denote the left hand side of (4) by $g(t)$ and the distribution of activity by $f(t)$. The reconstruction is to solve the following integral equation:

$$g(t) = \int_{-1}^{1} \frac{\cosh(\mu\tau)f(t-\tau)}{\pi\tau}d\tau.$$

As shown in Fig. 3, the function $f(t)$ has a support in $-1<t<1$. There is no loss of generality since shifting and scaling can always transform any support interval to $(-1,1)$.

If $g(t)$ is known for $-1<t<1$, the equation can be solved as in [19] and [17]. Unfortunately, for some geometries the function $g(t)$ is only available on a small interval $-1<a<t<d<1$. Then the algorithms in [19] and [17] do not guarantee a stable inversion. However, based on the work by Kudo et al [8], we found if the value of $f(t)$ in the interval $a<b<t<c<d$ is assumed to be known, then the inversion is available in (a,d).

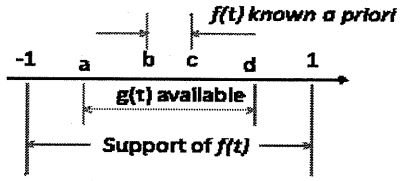

Figure 3. Illustration of intervals.

The reconstruction problem becomes:

$$g(t) = \int_{-1}^{1} \frac{\cosh(\mu\tau)f(t-\tau)}{\pi\tau}d\tau \quad . \quad (-1<a<t<d<1), \quad (5)$$

subject to $f(t) = f^{(p)}(t)$ for $(a<b<t<c<d)$.

According to [17], we know the inversion can be obtained by constructing a new function from $g(t)$:

$$\int_{-1}^{1} \frac{g(s)}{\pi(s-t)}\frac{\sqrt{1-t^2}}{\sqrt{1-s^2}}ds.$$

In this case, this function can be broken into two terms: $h_1(t)+h_2(t)$, where

$$h_1(t) = \int_{a}^{d} \frac{g(s)}{\pi(s-t)}\frac{\sqrt{1-t^2}}{\sqrt{1-s^2}}ds,$$

$$h_2(t) = \left(\int_{-1}^{a} . + \int_{d}^{1} .\right)\frac{g(s)}{\pi(s-t)}\frac{\sqrt{1-t^2}}{\sqrt{1-s^2}}ds.$$

The first term $h_1(t)$ is available from the truncated weighted Hilbert transform $g(t)$ for $a<t<d$, while the second term $h_2(t)$ remains unknown.

Since the function $f(t)$ is known for $b<t<c$, the second term in this interval can be represented as

$$h_2(t) = \left[\left((I+\Phi)f^{(p)}\right)\right](t) - h_1(t) \qquad \text{for} \qquad t\in(b,c).$$

Here, the operator Φ is the same as in [17] and I indicates the unity operator.

According to the continuity property of analytical functions, the function $h_2(t)$ can be analytically continued from the known interval (b, c) on the real axis to the larger interval (a, d) on the real axis. Since both $h_1(t)$ and $h_2(t)$ are uniquely determined for $t\in(a,d)$, function $f(t)$ is uniquely determined for $t\in(a,d)$. Then the projection onto convex sets (PCOS) method [22] was used to solve the integral equation in (5). Numerical results will be shown in the next section.

III. Numerical Results

In the fan-beam SPECT simulation study, the object image is chosen to be the modified Shepp-Logan phantom shown in Fig. 4. Uniform attenuation coefficient $\mu=0.15cm^{-1}$ was chosen to generate the truncated attenuated fan-beam data.

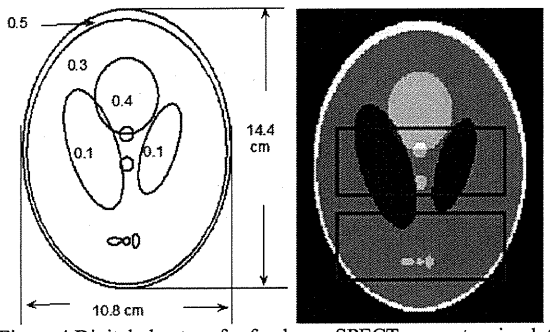

Figure 4 Digital phantom for fan-beam SPECT computer simulation. The square boxes in the right image indicate two regions-of-interest (ROIs).

In the reconstruction, first, differentiation followed by backprojection of truncated SPECT data was obtained. Then assuming the activity within a small part of the region-of-interest is known, the other part of the ROI was estimated using the PCOS method. The reconstructed image is shown in Fig. 5.

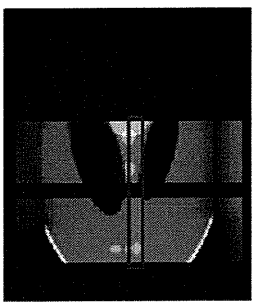

Figure 5: The reconstructed image for fan-beam geometry. The box indicates the region where the distribution is known *a priori*.

IV. Conclusion

This paper extended the work in [8] to SPECT imaging where uniform attenuation map is assumed. The interior problem was shown to be solvable given tiny *a priori* information. Reconstructions from simulated fan-beam data verify the theory.

The investigation of a pinhole system is presently undergoing. In the pinhole simulation, regularized maximum *a posteriori* (MAP) algorithm is used to reconstruct the simulated pinhole data. A low resolution reconstruction of the parallel beam collimated data is used as prior information.

References

[1] Iida H, Hayashida K, Nakazawa M and Katabuchi T, "Multicenter evaluation of quantitative SPECT reconstruction package – QSPECT & DTARG," *J. Nucl. Med.* 47 (Supplement 1), pp. 121, 2006.

[2] Rudzinski W, Swiat M, Tomaszewski M and Krejza J, "Cerebral hemodynamics and investigations of cerebral blood flow regulation," *Nucl Med Rev*, vol. 10, pp. 29-42, 2007.

[3] Imaizumi M, Kitagawa K, Hashikawa K, Oku N, Teratani T, Takasawa M, Yoshikawa T, Rishu P, Ohtsuki T, Hori M, Matsumoto M and Nishimura T, "Misery perfusion with split-dose ^{123}I-iodoamphetamine single-photon emission computed tomography in patients with carotid occlusive diseases," *Stroke*, vol. 33, pp. 2217-2223, 2002.

[4] Moriwaki H, Matsumoto M, Hashikawa K, Oku N, Ishida M, Seike Y, Fukuchi K, Hori M and Nishimura T, "Iodine-123-iomazenil and iodine-123-Iodoamphetamine SPECT in major cerebral artery occlusive disease," *J Nucl Med*, vol. 39, pp. 1348-1353, 1998.

[5] Tsuchida T, Yonekura Y, Sadato N, Takahashi N, Yamamoto K and Ishii Y, "Prediction of improvement of cerebral perfusion with I-123 iomazenil SPECT," *Annals of Nucl. Med.*, vol. 13, pp. 265-268, 1999.

[6] Dargham A, Larulle M, Seibyl J, Rattner Z, Baldwin R M, Zoghbi S S, Zea-Ponce Y, Bremner J D, Hyde T M, Charney D S, Hoffer P B and Innis R B, "SPECT measurement of benzodiazepine receptors in human brain with iodine-123-iomazenil: kinetic and equilibrium paradigms," *J. Nucl. Med.*, vol. 35, pp. 228-238, 1994.

[7] Natterer F, *The Mathematics of Computerized Tomography* (SIAM), 1986.

[8] Kudo H, Courdurier M, Noo F and Defrise M, "Tiny *a proiri* knowledge solves the interior problem in computed tomography," *Phys. Med. Bio.*, vol. 53, pp. 2207-2231, 2008.

[9] Noo F, Clackdoyle R and Pack J D, "A two-step Hilbert transform method for 2D image reconstruction," *Phys. Med. Biol.*, vol. 49, pp. 3903-3923, 2004.

[10] Zou Y and Pan X, "Exact image reconstruction on PI-lines from minimum data in helical cone-beam CT," *Phys. Med. Biol.*, vol. 49, pp. 941-959, 2004.

[11] Pack J D, Noo F and Clackdoyle R, "Cone-beam reconstruction using the backprojection of locally-filtered projections," *IEEE Trans. Med. Imag.*, vol. 24, pp. 70-85, 2005.

[12] Pack J D and Noo F, "Cone-beam reconstruction using 1D filtering along the projection of M-lines," *Phys. Med. Biol.*, vol. 49, pp. 2317-2336, 2004.

[13] Ye Y and Wang G, "Filtered backprojection formula for exact image reconstruction from cone-beam data along a general scanning curve," *Med. Phys.*, vol. 32, pp. 42-48, 2005.

[14] Zou Y and Pan X, "Image reconstruction on PI-lines by use of filtered backprojection in helical cone-beam CT," *Phys. Med. Biol.*, vol. 49, pp. 2717-2731, 2004.

[15] Zou Y and Pan X, "An extended data function and its generalized backprojection for image reconstruction in helical cone-beam CT," *Phys. Med. Biol.*, vol. 49, pp. N3837, 2004.

[16] Huang Q, You J, Zeng G L and Gullberg G T, "Exact Reconstruction From Uniformly Attenuated Helical Cone-Beam projections in SPECT," LBNL Technical Report, LBNL-1359E, Lawrence Berkeley National Lab, Berkeley, USA., 2008.

[17] Huang Q, You J, Zeng G L, and Gullberg G T, "Reconstruction from uniformly attenuated SPECT partial-scan projection data using DBH method," IEEE Trans. Med. Imag., vol. 28, pp. 17-29, 2009.

[18] Noo F and Pack J D, "Theory for image reconstruction from divergent beam projections in SPECT," *IEEE Nuclear Science Symposium Conference Record*, vol. 6, pp. 3449-3452, 2006.

[19] Noo F, Defrise F, Pack J and Clackdoyle R, "Image reconstruction from truncated data in SPECT with uniform attenuation," *Inverse Problems*, vol. 23, pp. 645-667, 2007.

[20] Rullgard H, "An explicit inversion formula for the exponential Radon transform using data from 180 degrees," (Preprint in 2002 Sep) *Ark. Math.*, vol. 42, pp. 353-362, 2004.

[21] Liang Z, Ye J and Harrington D P, "Quantitative brain SPECT in three dimensions: an analytical approach without transmission scans," *Three-Dimensional Image Reconstruction in Radiology and Nuclear Medicine*, Kluwer Academic Publishers, pp. 117-132, 1996.

[22] Youla D C and Webb H, "Image restoration by the method of convex projections: Part I. Theory," *IEEE Trans Med. Imag.*, vol. 1, pp. 81–94, 1982.

Therapeutic efficacy of a polymeric micellar doxorubicin infused by convection-enhanced delivery against intracranial 9L brain tumor models

Tomoo Inoue, Yoji Yamashita, Masamichi Nishihara, Shinichiro Sugiyama, Yukihiko Sonoda, Toshihiro Kumabe, Masayuki Yokoyama, and Teiji Tominaga

Department of Neurosurgery, Tohoku University Graduate School of Medicine, Sendai (T.I., Y.Y., S.S., Y.S., T.K., T.T.), and Yokoyama Nano-medical Polymers Project, Kanagawa Academy of Science and Technology, Kawasaki (M.N., M.Y.); Japan

Convection-enhanced delivery (CED) with various drug carrier systems has recently emerged as a novel chemotherapeutic method to overcome the problems of current chemotherapies against brain tumors. Polymeric micelle systems have exhibited dramatically higher in vivo antitumor activity in systemic administration. This study investigated the effectiveness of CED with polymeric micellar doxorubicin (DOX) in a 9L syngeneic rat model. Distribution, toxicity, and efficacy of free, liposomal, and micellar DOX infused by CED were evaluated. Micellar DOX achieved much wider distribution in brain tumor tissue and surrounding normal brain tissue than free DOX. Tissue toxicity increased at higher doses, but rats treated with micellar DOX showed no abnormal neurological symptoms at any dose tested (0.1–1.0 mg/ml). Micellar DOX infused by CED resulted in prolonged median survival (36 days) compared with free DOX (19.6 days; $p = 0.0173$) and liposomal DOX (16.6 days; $p = 0.0007$) at the same dose (0.2 mg/ml). This study indicates the potential of CED with the polymeric micelle drug carrier system for the treatment of brain tumors.
Neuro-Oncology 11, 151–157, 2009 (Posted to Neuro-Oncology [serial online], Doc. D08-00039, August 28, 2008. URL http://neuro-oncology.dukejournals.org; DOI: 10.1215/15228517-2008-068)

Keywords: brain tumors, convection-enhanced delivery, doxorubicin, drug delivery system, polymeric micelle

Received February 18, 2008; accepted July 22, 2008.

Address correspondence to Yoji Yamashita, Department of Neurosurgery, Tohoku University Graduate School of Medicine, 1-1, Seiryo-machi, Aoba-ku, Sendai 980-8574, Japan (yoji@nsg.med.tohoku.ac.jp).

Convection-enhanced delivery (CED) is a promising local delivery technique using bulk flow to deliver low-molecular-weight and macromolecular drugs directly to targeted sites in clinically significant volumes of tissue and to achieve wider volumes of distribution compared with simple diffusion techniques.[1] CED bypasses the blood–brain barrier that prevents most anticancer drugs from penetrating into the CNS, delivers a high concentration of therapeutic agents to the targeted site, and minimizes systemic exposure, resulting in fewer side effects.[1] Many antineoplastic drugs,[2–5] including immunotoxins and boronated drugs,[6,7] have been administered using CED, with promising outcomes in animal studies. The problems include rapid drug clearance from the tumor interstitium,[6] no selective accumulation in targeted tissues,[7] and brain damage caused by highly cytotoxic agents with extensive distribution in the CNS.[2–5] Consequently, novel drug delivery systems are necessary to achieve the highest possible therapeutic index against tumor cells over healthy neuronal cells.[8,9]

Incorporation or attachment of low-molecular-weight anticancer drugs into drug carriers with high molecular

weight and hydrophilicity may provide substantial inhibition of drug clearance from the tumor interstitium, in contrast to low-molecular-weight drugs that are cleared very rapidly by active transport via proteins such as P-glycoprotein as well as by passive diffusive transport through the lipid bilayer of the endothelium. The drug carrier systems also offer the advantage of sustained drug release, as prolonged exposure time is more important than the peak concentration factor for many anticancer drugs. However, only liposomes have been studied as drug carriers in combination with CED.[8–12]

Polymeric micelles are an assembly of synthetic polymers, most typically block copolymers with both hydrophobic and hydrophilic blocks. Polymeric micelle carrier systems were first studied for targeting solid tumors by intravenous injection.[13–16] Polymeric micelle carrier systems are electrically neutral and so have the so-called stealth property that evades rapid clearance at the reticuloendothelial systems,[17] which substantially improves targeting of murine solid tumors due to the enhanced permeability and retention effect that depends on the hyperpermeable vasculature and absence of effective lymphatic drainage that prevents efficient clearance of micromolecules in the solid tumor tissues.[18] Polymeric micelles incorporating micellar doxorubicin (DOX) were initially developed to enhance the safety and efficacy of conventional DOX.[13] Various micelle-encapsulated cytotoxic agents are currently undergoing clinical evaluation of systemic administration, including DOX,[9] paclitaxel,[19] cisplatin,[20] camptothecin,[21] and the camptothecin derivative SN-38.[22] In contrast, local delivery of polymeric micelle systems for the treatment of brain tumors remains relatively unexplored.

The present study evaluated the therapeutic possibilities of micellar DOX in a 9L syngeneic rat brain tumor model.

Materials and Methods

Preparation of Agents

Doxorubicin hydrochloride was purchased from Mercian Corp. (Tokyo, Japan). Stock solutions of free DOX were prepared by diluting DOX in dimethyl sulfoxide to a concentration of 50 mg/ml. The infusion solution of free DOX was made by diluting the stock solution with phosphate-buffered saline (PBS). Liposomal DOX (Doxil) was obtained from Alza Pharmaceuticals (Mountain View, CA, USA). Micellar DOX was prepared by the previously reported method in a slight modification only in high-performance liquid chromatography (HPLC) analysis conditions.[14–16] In brief, DOX was chemically conjugated to the aspartic acid residue of poly(ethylene glycol)-b-poly(aspartic acid) block copolymer. The hydrophobicity of the DOX-conjugated poly(aspartic acid) block results in the formation of a polymeric micelle structure. This conjugate block copolymer was used to form empty polymeric micelles in this study because this type of micelle does not contain unbound DOX that is important in cytotoxic activity. Free DOX was incorporated into empty polymeric micelles to form pharmacologically active polymeric micelles that contain free DOX in the micelle inner core. The poly(ethylene glycol) block had a molecular weight of 12 kDa and contained 22 aspartic acid units as determined by ^{1}H-nuclear magnetic resonance spectrum in D_2O. DOX was chemically conjugated to 59% of the aspartic acid residues, and the micelles contained 13 wt% free DOX. The amounts of the chemically conjugated DOX and the physically entrapped DOX were determined by a reverse-phase HPLC according to methods previously reported.[15,16] The empty polymeric micelles (DOX was not physically entrapped) chemically conjugated DOX molecules to 68% of the aspartic acid residues. The infusion solution for micellar DOX, PBS, had no toxicity when 20 µl was infused by CED (preliminary data not shown).

Tumor Cell Lines

9L gliosarcoma cells (American Type Culture Collection, Rockville, MD, USA) were maintained as monolayers in a complete medium consisting of Eagle's minimal essential medium supplemented with 10% fetal calf serum, nonessential amino acids, and 100 U/ml penicillin G. Cells were cultured at 37°C in a humidified atmosphere consisting of 95% air and 5% CO_2.

Animals and Intracranial Syngeneic Transplantation Technique

All protocols utilized in the animal studies were approved by the Institute for Animal Experimentation of Tohoku University Graduate School of Medicine. Male Fischer 344 rats weighing 150–200 g and normal male Sprague-Dawley rats weighing approximately 150–200 g were purchased from Charles-River Laboratories (Charles-River Japan Inc., Tsukuba, Japan). For the intracranial syngeneic tumor model, 9L gliosarcoma cells were harvested by trypsinization, washed once with Hanks' balanced salt solution without Ca^{2+} and Mg^{2+} (HBSS), and resuspended in HBSS for implantation. Cells (5×10^5) in 10 µl HBSS were implanted into the striatal region of the rat brains as follows. The rats under deep isoflurane anesthesia were placed in a small-animal stereotactic frame (David Kopf Instruments, Tujunga, CA, USA). A sagittal incision was made to expose the cranium, followed by a burr hole in the skull at 0.5 mm anterior and 3 mm lateral from the bregma using a small dental drill. Cell suspension (5 µl) was injected over 2 min at a depth of 4.5 mm from the brain surface; after a 2-min wait, another 5 µl was injected over 2 min at a depth of 4.0 mm, and after a final 2-min wait, the needle was removed and the wound was sutured.

CED Infusion

CED of PBS, free DOX, liposomal DOX, and micellar DOX was performed as described previously.[9,11] The infusion system consisted of a reflux-free step design infusion cannula[23] connected to a loading line (containing 20 µl PBS, free DOX, liposomal DOX, or micellar

DOX solutions) and an olive oil infusion line. A 1-ml syringe (filled with oil) was mounted onto a microinfusion pump (BeeHive; Bioanalytical Systems, West Lafayette, IN, USA) to regulate the flow of fluid through the system. Based on chosen coordinates, the infusion cannula was mounted onto a stereotactic holder and guided to the target region of the brain through burr holes made in the skull (see below). The infusion rates followed the following ascending pattern to deliver the total 20-µl infusion volume: 0.2 µl/min (15 min) + 0.5 µl/min (10 min) + 0.8 µl/min (15 min).

Evaluation of Distribution of Micellar DOX in Normal Rodent CNS

Normal Sprague-Dawley rats (five rats in each group) received CED using free DOX (2 mg/ml DOX in 20 µl solution), liposomal DOX (20 µl solution containing 2 mg/ml DOX equivalent), and micellar DOX (20 µl solution containing 2 mg/ml physically entrapped DOX and 4.3 mg/ml chemically conjugated DOX equivalent), and empty polymeric micelles (20 µl solution containing 7.9 mg/ml chemically conjugated DOX equivalent) and were euthanized immediately after CED. The brains were harvested, frozen in isopentane chilled in dry ice, and cut into serial coronal sections (25 µm) with a cryostat. DOX fluoresces under UV illumination, so the areas of distribution could be visualized by fluorescence microscopy and captured with a charged-coupled device camera with a fixed aperture. The empty polymeric micelles were also fluorescent in a similar manner to the micellar DOX, since the empty polymeric micelles contained chemically conjugated DOX molecules that were almost equivalent in their fluorescent behavior to physically entrapped DOX of the micellar DOX. The volume of distribution was analyzed with a Macintosh-based image-analysis system (NIH Image 1.62; NIH, Bethesda, MD, USA) as described previously.[24]

Evaluation of Distribution of Micellar DOX in Rats with 9L Intracranial Tumors

Fischer 344 rats (four rats in each group) with 9L intracranial tumors received CED using micellar DOX and free DOX (20 µl solution containing 2 mg/ml DOX equivalent) 7 days after tumor cell implantation. Rats were euthanized immediately after CED. The brains were harvested, frozen in isopentane chilled in dry ice, and cut into serial coronal sections (25 µm) with a cryostat.

Toxicity Tests of Micellar DOX

Normal Sprague-Dawley rats (five rats in each group) received a single CED infusion of free DOX, liposomal DOX, micellar DOX, and empty polymeric micelles (20 µl solutions containing 0.1, 0.2, 0.4, or 1.0 mg/ml free DOX equivalent). Rats were monitored daily for survival and general health (alertness, grooming, feeding, excreta, skin, fur, mucous membrane conditions, ambulation, breathing, and posture) and weekly for weight. The rats in each group were euthanized 3 weeks after the CED treatment, and their brains were removed, fixed, cut into sections (5 µm), and stained with hematoxylin and eosin (H&E).

Survival Studies

Fifty-two Fischer 344 rats with 9L tumor cells were randomly assigned to four groups: (1) the control group that received PBS (20 µl solution; $n = 17$), (2) free DOX (0.2 mg/ml DOX in 20 µl solution; $n = 10$), (3) liposomal DOX (20 µl solution containing 0.2 mg/ml DOX equivalent; $n = 14$), and (4) micellar DOX (20 µl solution containing 0.2 mg/ml physically entrapped free DOX equivalent; $n = 11$). Seven days after tumor cell implantation, a single CED infusion was performed for each group. Rats were monitored daily for survival and general health, and weekly for weight. The study was terminated 90 days after tumor implantation. The surviving animals were euthanized and their brains stained with H&E. Survival was expressed as a Kaplan-Meier curve. Survival between the treatment groups was compared with a log-rank test.

Results

Evaluation of Distribution of Micellar DOX in Normal Rodent CNS

Compared with free DOX (Fig. 1a), intrastriatal administration of liposomal DOX (Fig. 1b), micellar DOX (Fig. 1c), and empty polymeric micelles (Fig. 1d) via CED (20 µl volume) produced extensive and diffuse distribution in the striatum. The mean volumes of distribution of free DOX, liposomal DOX, micellar DOX, and empty polymeric micelles in normal rat brains were 13.91 ± 1.23 mm^3 (range, 12.12–15.32 mm^3), 64.25 ± 7.83 mm^3 (54.76–77.40 mm^3), 60.54 ± 5.71 mm^3 (54.40–64.25 mm^3), and 54.74 ± 4.39 mm^3 (50.30–58.97 mm^3), respectively (Fig. 1e). A significant difference was observed between free DOX and micellar DOX ($p = 0.009$), but not between liposomal DOX and micellar DOX ($p = 0.465$).

Evaluation of Distribution of Micellar DOX in Rats with 9L Tumors

Examination of representative rat brain sections at 1-mm intervals confirmed successful formation of the tumor tissue. Fluorescent detection of DOX in the same sections revealed poor distribution of free DOX (Fig. 2a) but distribution of micellar DOX over almost the entire tumor mass, including the surrounding tumor margins (Fig. 2b). The findings were consistent in all four rats examined from this group.

Toxicity of Micellar DOX in Normal Rodent CNS

Rats euthanized 3 weeks after infusion with 0.2 (Fig. 3a, center), 0.4 (Fig. 3a, right), and 1.0 (data not shown) mg/ml micellar DOX showed tissue damage at the infusion

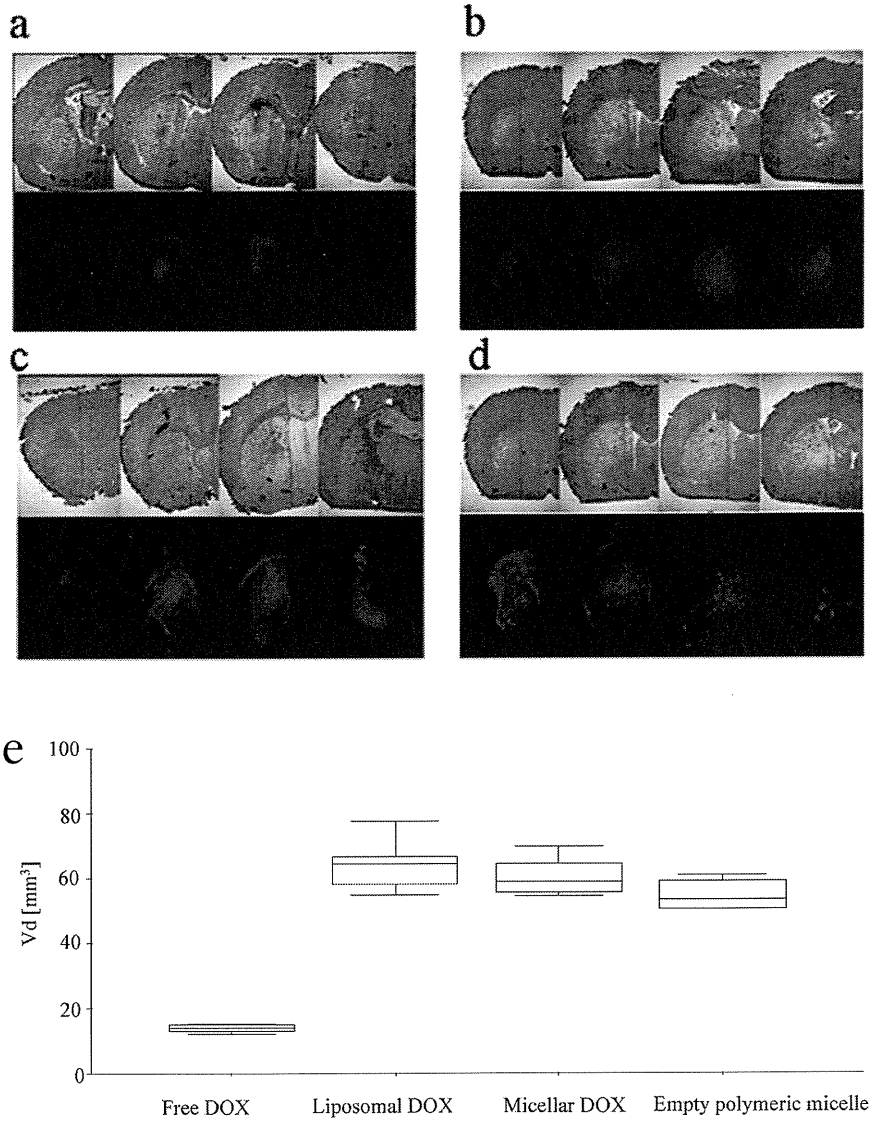

Fig. 1. Evaluation of distribution of micellar DOX in normal rats. Sequential hematoxylin and eosin-stained sections 25 μm thick at 1-mm intervals reveal the tumor (top). The sections were examined with a fluorescence microscope to detect the fluorescence generated by DOX (bottom). Compared with free DOX (a), liposomal DOX (b), micellar DOX (c), and empty polymeric micelles (d) produced extensive and diffuse distribution in the striatum. (e) Median values and the 75% quartiles of volume distribution (Vd) after infusion of free DOX, liposomal DOX, micellar DOX, and empty polymeric micelles. The difference in the distribution between free DOX and micellar DOX was statistically significant ($p = 0.009$, as analyzed by Mann-Whitney U-test), but differences in the distribution among liposomal DOX, micellar DOX, and empty polymeric micelles were not.

site but did not develop neurological symptoms. Rats that received 0.1 mg/ml micellar DOX (Fig. 3a, left) showed negligible tissue damage and survived without neurological symptoms. Rats infused with 0.1 (Fig. 3b, left) and 0.4 (Fig. 3b, right) mg/ml free DOX showed tissue damage without neurological symptoms. Rats infused with 0.1 (Fig. 3c, left) and 0.4 (Fig. 3c, right) mg/ml liposomal DOX revealed less tissue damage. Therefore, the maximum tolerated dose of micellar DOX was established as below 0.2 mg/ml. Rats treated with empty polymeric micelles showed no toxicity (data not shown).

Antitumor Efficacy of Micellar DOX Treatment

Rats in the control group (Fig. 4a) were all euthanized at 10–21 days after tumor cell implantation due to neurological symptoms indicative of tumor progression. Median survival for this group was 16.9 days. Rats that received CED of free DOX (Fig. 4b) were euthanized due to neurological complications indicative of tumor progression at 16–33 days after tumor cell implantation. Median survival for this group was 19.6 days. Rats that received CED of 0.2 mg/ml liposomal DOX

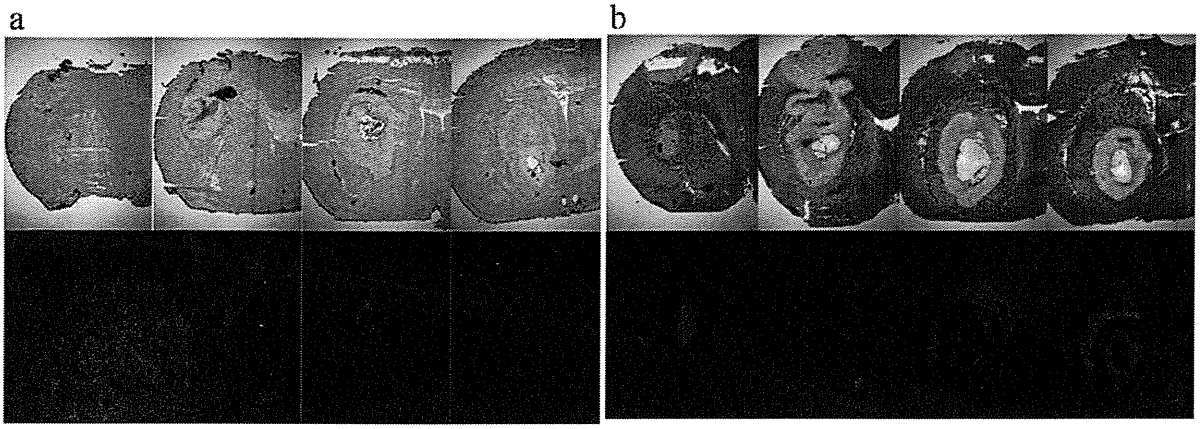

Fig. 2. Evaluation of distribution of micellar DOX in rats with 9L tumors. Seven days after tumor cell implantation, 2 mg/ml free DOX or micellar DOX was infused intratumorally by CED. Rats were euthanized 1 h after CED, and the brains were sectioned on a cryostat. Sequential hematoxylin and eosin-stained sections 25 μm thick at 1-mm intervals reveal the tumor (top). The same sections were examined with a fluorescence microscope to detect the fluorescence generated by DOX (bottom). Free DOX had poor distribution (a), whereas micellar DOX achieved coverage of almost the entire tumor mass, including the surrounding tumor margins (b). The findings were consistent in all four animals.

(Fig. 4c) were euthanized at 10–27 days after tumor cell implantation. Median survival for this group was 16.6 days. Formation of large tumors was verified in all rats euthanized in these three groups. Nine of the 11 rats that received CED of 0.2 mg/ml micellar DOX (Fig. 4d) were euthanized at 15–43 days after tumor cell implantation due to neurological symptoms, but the other two rats survived until termination of the study at 90 days. Median survival for this group was 36 days. The survival time after CED with 0.2 mg/ml micellar DOX was significantly greater than after CED with free DOX (p = 0.0173) or liposomal DOX (p = 0.0007). Although the rats in the control group had histological signs of tumor in the brain (Fig. 4e), only a small amount of brain damage was observed in the surviving two rats that received micellar DOX (Fig. 4f).

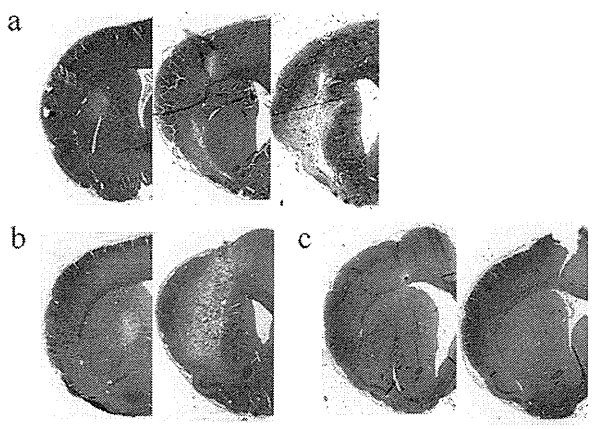

Fig. 3. Toxicity at different drug concentrations. (a) Rats infused with 0.1 mg/ml micellar DOX (left) survived without neurological symptoms and negligible tissue damage. Rats infused with 0.2 (center) and 0.4 (right) mg/ml micellar DOX showed significant tissue damage at the infusion site but did not develop neurological symptoms. (b) Rats infused with 0.1 (left) and 0.4 (right) mg/ml free DOX demonstrated tissue damage without neurological symptoms. (c) Rats infused with 0.1 (left) and 0.4 (right) mg/ml liposomal DOX revealed less tissue damage, which might reflect the poor drug release.

Discussion

The present study found that liposomal DOX and micellar DOX had similar extensive distributions in the normal rat brain and were far more widely distributed than free DOX. This study also showed distribution of micellar DOX over almost the entire tumor area, including the margins. CED distribution in CNS is significantly increased if the infusate is more hydrophilic, which implies less tissue affinity.[9,11] Furthermore, polyethylene glycol encapsulation provides steric stabilization, reduces surface charge, and achieves better distribution in brain.[9] The poorer brain distribution observed with hydrophobic or cationic infusate can be completely overcome by polyethylene glycol encapsulation.[9]

Delivery pattern of micellar DOX was expected to avoid the high peak concentrations of free DOX potentially associated with toxicity.[13,25] However, evaluation of the toxicity in normal rat brain found that 0.2 mg/ml micellar DOX caused a lesion similar to that caused by 0.2 mg/ml free DOX, although no difference in toxicity was observed. In contrast, 0.2 mg/ml liposomal DOX showed no toxicity, which might reflect poor release of the cytotoxic agent. These findings indicate that the safety of micellar DOX in CED could be achieved by optimization of drug release to avoid the high concentrations that trigger nonspecific toxicity. Micellar systems, relative to liposomal systems, offer the advantage of adjustable drug release based on the properties of the

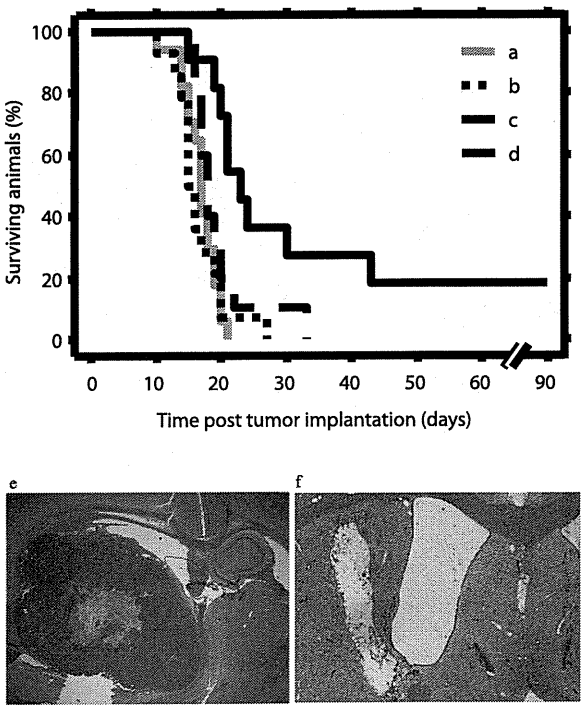

Fig. 4. Survival study. (a–d) Outcome for rats bearing 9L tumors with single CED infusion of saline (a), free DOX (b), liposomal DOX (c), and micellar DOX (d). Seven days after tumor implantation within the brain, rats were treated with 0.2 mg/ml of each agent. Median survival for the groups were 16.9 days (a), 19.6 days (b), 16.6 days (c), and 36 days (d). Statistically significant differences were observed between free DOX and micellar DOX ($p = 0.0173$) and between liposomal DOX and micellar DOX ($p = 0.0007$). (e and f) Histological examination found tumor formation in the control group (e) and brain damage in rats receiving micellar DOX (f).

micelle inner core,[13–16,25] but further development of micellar systems for use with CED is required.

The present study found that CED with 0.2 mg/ml micellar DOX significantly prolonged survival in rats with intracranial 9L glioma, compared with CED with 0.2 mg/ml free DOX and liposomal DOX, which is known to show efficient targeting to solid tumors by systemic injection like micellar DOX. Liposomal DOX does not release DOX efficiently because of excessive stable incorporation in the lipid bilayer,[17] which probably accounts for the absence of significant increase in efficacy against rapidly growing 9L syngeneics compared with free DOX.

The polymeric micelle system has three advantages as a drug carrier compared with the liposome drug carrier. First, polymeric micelles can incorporate hydrophobic drugs into the inner core phase, to high loadings such as 30 wt% without losing targeting potential. In contrast, the liposomal system may easily lose targeting ability at high drug loadings because the hydrophobic drug must be incorporated into the very thin lipid bilayer. Second, polymers may be based on many chemical structures with various physical characteristics such as crystalline and glassy, so the drug release rate can be adjusted in a very wide range from minutes to days. Finally, micelle diameters can be tightly controlled in a range from 10 nm to 100 nm, choosing the appropriate chemical structures and chain lengths of polymers. The polymeric micelle can obtain this size control among many types of drug carriers. Consequently, the micelle system has high potential for specific adjustment to the treatment of various CNS tumors by CED infusion. Furthermore, micellar systems could be used in monitoring drug distribution by using micelles containing a marker for imaging.[23,24] The present findings indicate the significant potential of micellar drugs for the treatment of malignant glioma.

References

1. Bobo RH, Laske DW, Akbasak A, Morrison PF, Dedrick RL, Oldfield EH. Convection-enhanced delivery of macromolecules in the brain. *Proc Natl Acad Sci USA.* 1994;91:2076–2080.
2. Bruce JN, Falavigna A, Johnson JP, et al. Intracerebral clysis in a rat glioma model. *Neurosurgery.* 2000;46:683–691.
3. Degen JW, Walbridge S, Vortmeyer AO, Oldfield EH, Lonser RR. Safety and efficacy of convection-enhanced delivery of gemcitabine or carboplatin in a malignant glioma model in rats. *J Neurosurg.* 2003;99:893–898.
4. Kaiser MG, Parsa AT, Fine RL, Hall JS, Chakrabarti I, Bruce JN. Tissue distribution and antitumor activity of topotecan delivered by intracerebral clysis in a rat glioma model. *Neurosurgery.* 2000;47:1391–1399.
5. Vogelbaum MA. Convection enhanced delivery for treating brain tumors and selected neurological disorders: symposium review. *J Neurooncol.* 2007;83:97–109.
6. Kunwar S, Prados MD, Chang SM, et al. Cintredekin Besudotox Intraparenchymal Study Group. Direct intracerebral delivery of cintredekin besudotox (IL13-PE38QQR) in recurrent malignant glioma: a report by the Cintredekin Besudotox Intraparenchymal Study Group. *J Clin Oncol.* 2007;25:837–844.
7. Wu G, Yang W, Barth RF, et al. Molecular targeting and treatment of an epidermal growth factor receptor-positive glioma using boronated cetuximab. *Clin Cancer Res.* 2007;13:1260–1268.
8. Krauze MT, Noble CO, Kawaguchi T, et al. Convection-enhanced delivery of nanoliposomal CPT-11 (irinotecan) and PEGylated liposomal doxorubicin (Doxil) in rodent intracranial brain tumor xenografts. *Neuro-Oncology.* 2007;9:393–403.
9. Yamashita Y, Krauze MT, Kawaguchi T, et al. Convection-enhanced delivery of a topoisomerase I inhibitor (nanoliposomal topotecan) and a topoisomerase II inhibitor (pegylated liposomal doxorubicin) in intracranial brain tumor xenografts. *Neuro-Oncology.* 2007;9:20–28.

10. Noble CO, Krauze MT, Drummond DC, et al. Novel nanoliposomal CPT-11 infused by convection-enhanced delivery in intracranial tumors: pharmacology and efficacy. *Cancer Res.* 2006;66:2801–2806.
11. Saito R, Bringas JR, McKnight TR, et al. Distribution of liposomes into brain and rat brain tumor models by convection-enhanced delivery monitored with magnetic resonance imaging. *Cancer Res.* 2004;64:2572–2579.
12. MacKay JA, Deen DF, Szoka FC Jr. Distribution in brain of liposomes after convection enhanced delivery; modulation by particle charge, particle diameter, and presence of steric coating. *Brain Res.* 2005;1035:139–153.
13. Yokoyama M, Miyauchi M, Yamada N, et al. Characterization and anticancer activity of the micelle-forming polymeric anticancer drug Adriamycin-conjugated poly(ethylene glycol)-poly(aspartic acid) block copolymer. *Cancer Res.* 1990;50:1693–1700.
14. Yokoyama M, Fukushima S, Uehara R, et al. Characterization of physical entrapment and chemical conjugation of Adriamycin in polymeric micelles and their design for in vivo delivery to a solid tumor. *J Control Release.* 1998;50:79–92.
15. Fukushima S, Machida M, Akutsu T, et al. Role of Adriamycin and Adriamycin dimer in antitumor activity of the polymeric micelle carrier system. *Colloids Surf B Biointerfaces.* 1999;16:227–236.
16. Yokoyama M, Okano T, Sakurai Y, et al. Selective delivery of Adriamycin to a solid tumor using a polymeric micelle carrier system. *J Drug Target.* 1999;7:171–186.
17. Tsukioka Y, Matsumura Y, Hamaguchi T, et al. Pharmaceutical and biomedical differences between micellar doxorubicin (NK911) and liposomal doxorubicin (Doxil). *Jpn J Cancer Res.* 2002;93:1145–1153.
18. Greish K. Enhanced permeability and retention of macromolecular drugs in solid tumors: a royal gate for targeted anticancer nanomedicines. *J Drug Target.* 2007;15:457–464.
19. Hamaguchi T, Kato K, Yasui H, et al. A phase I and pharmacokinetic study of NK105, a paclitaxel-incorporating micellar nanoparticle formulation. *Br J Cancer.* 2007;97:170–176.
20. Uchino H, Matsumura Y, Negishi T, et al. Cisplatin-incorporating polymeric micelles (NC-6004) can reduce nephrotoxicity and neurotoxicity of cisplatin in rats. *Br J Cancer.* 2005;93:678–687.
21. Kawano K, Watanabe M, Yamamoto T, et al. Enhanced antitumor effect of camptothecin loaded in long-circulating polymeric micelles. *J Control Release.* 2006;112:329–332.
22. Koizumi F, Kitagawa M, Negishi T, et al. Novel SN-38-incorporating polymeric micelles, NK012, eradicate vascular endothelial growth factor-secreting bulky tumors. *Cancer Res.* 2006;66:10048–10056.
23. Amirbekian V, Lipinski MJ, Briley-Saebo KC, et al. Detecting and assessing macrophages in vivo to evaluate atherosclerosis noninvasively using molecular MRI. *Proc Natl Acad Sci USA.* 2007;104:961–966.
24. Lepage M, Jiang J, Babin J, Qi B, Tremblay L, Zhao Y. MRI observation of the light-induced release of a contrast agent from photo-controllable polymer micelles. *Phys Med Biol.* 2007;52:249–255.
25. Yokoyama M, Okano T, Sakurai Y, Ekimoto H, Shibazaki C, Kataoka K. Toxicity and antitumor activity against solid tumors of micelle-forming polymeric anticancer drug and its extremely long circulation in blood. *Cancer Res.* 1991;51:3229–3236.

Journal of Controlled Release 136 (2009) 14–20

Contents lists available at ScienceDirect

Journal of Controlled Release

journal homepage: www.elsevier.com/locate/jconrel

Preparation and in vivo imaging of PEG-poly(L-lysine)-based polymeric micelle MRI contrast agents

Kouichi Shiraishi [a], Kumi Kawano [b], Takuya Minowa [b], Yoshie Maitani [b], Masayuki Yokoyama [a,*]

[a] Kanagawa Academy of Science and Technology, Yokoyama "Nano-medical Polymers" Project, KSP East 404, Sakado 3-2-1, Takatsu-ku, Kawasaki, Kanagawa 213-0012, Japan
[b] Institute of Medicinal Chemistry, Hoshi University, 2-4-41 Ebara, Shinagawa-ku, Tokyo 142-8501, Japan

ARTICLE INFO

Article history:
Received 24 October 2008
Accepted 17 January 2009
Available online 23 January 2009

Keywords:
Polymeric micelle
MRI contrast agent
Long circulation
Tumor imaging
Poly(ethylene glycol)-b-poly(L-lysine)

ABSTRACT

A polymeric micelle drug carrier system was applied to the targeting of an MRI (magnetic resonance imaging) contrast agent. A block copolymer, PEG-*b*-poly(L-lysine), was used for conjugation of gadolinium ions through chelating moieties, DOTA. The DOTA moieties were successfully conjugated to all primary amine groups of the lysine residues. The obtained block copolymer, PEG-*b*-poly(L-lysine-DOTA), formed a polymeric micelle. The polymeric micelle structure was maintained even after partial gadolinium chelation (~40%) to the DOTA moieties. The prepared polymeric micelle MRI contrast agent was injected into a mouse tail vein at a dose of 0.05 mmol Gd/kg. The polymeric micelle-based MRI contrast agent exhibited stable blood circulation. A considerable amount (6.1 ± 0.3% of ID/g of the polymeric micelle) was found to accumulate at solid tumors 24 h after intravenous injection by means of the EPR effect. An MRI analysis revealed that the signal intensity of the tumor was enhanced 2.0-fold by the use of this contrast agent.

1. Introduction

Various types of nano-sized drug carriers including linear synthetic polymers, dendrimers, proteins, liposomes, and polymeric micelles have been investigated for anti-cancer drug targeting to solid tumor sites for improvements in cancer chemotherapy [1,2]. Among these nano-sized carrier systems, polymeric micelles have been studied with a focus on encapsulation of hydrophobic drugs [3]. Most typically, polymeric micelles are constituted of block copolymers having a hydrophilic chain such as PEG and a hydrophobic chain. The hydrophobic chain can form a hydrophobic inner core that incorporates hydrophobic drugs. A strong advantage of the polymeric micelles is their high structural stability in the bloodstream and their very small size, being in a range of 10–100 nm. This size range is preferable for the passive targeting of solid tumors by means of the EPR (enhanced permeability and retention) effect [3]. Successful tumor-targeting-carrier systems include the adriamycin-incorporated polymeric micelle system [1], which involves a metal complex drug-incorporated (e.g., cisplatin-incorporated) polymeric system [4–6].

The recent study reported that several nano-sized-carrier system and, in particular, diagnostic imaging agents rest on drug-targeting methodology. Magnetic resonance imaging (MRI) is a non-invasive imaging modality for diagnosis. Owing to rapid developments in temporal and spatial resolution, the value of MRI has grown greater in recent decades. Nowadays, much attention is given to MRI contrast agents both of low molecular weight and of macromolecule status for their ability to improve MRI signals.

Paramagnetic metal complexes, such as the gadolinium (III) ion–DTPA complex, are widely used in clinical diagnosis. Such gadolinium complexes enhance T_1-weighted images by shortening the T_1-relaxation time of the water protons. Linear polymers such as dextran [7,8], poly(L-lysine) [9,10], poly(glutamic acid) [11–13], and poly[N-(2-hydroxypropyl)methacrylamide] [14] have been investigated as possible for carriers of the gadolinium complexes. Dendrimers, which possess well-defined structures and accurate molecular weights, have also attracted much attention as carriers of MRI contrast agents because dendrimers' biodistribution were depend on the generations [15–17].

Polymeric micelle-based MRI contrast agents also have a potential as MRI contrast agents. Because the polymeric micelle is an associate of many block copolymer chains, block copolymers with well-controlled molecular weight can be excreted through kidney filtration after dissociation of the polymeric micelles into block copolymer chains. Therefore, a low risk of chronic toxicity is expected to present itself and is expected to stem from polymeric micelles' complete excretion over a long time period. On the other hand, polymeric micelles can exhibit a preferential pharmacokinetic profile in a defined time period required for the targeting of tumors. In a previous report, we prepared a polyion complex micelle from charged block copolymers and counter ionic polymers [18]. This polymeric micelle MRI contrast agent possessed the characteristic of changeable T_1-relaxivity: The polymeric micelle exhibited a lower T_1-relaxivity than did block copolymer chains having dissociated from the micelle. This changeable character can be utilized as a tumor-specific MRI contrast

* Corresponding author. Tel.: +81 44 819 2093; fax: +81 44 819 2095.
E-mail address: yp-yokoyama2093ryo@newkast.or.jp (M. Yokoyama).

0168-3659/$ – see front matter © 2009 Elsevier B.V. All rights reserved.
doi:10.1016/j.jconrel.2009.01.010

with a high MRI contrast (in dissociate form) at tumor tissues and a low MRI contrast (in micelle form) in the bloodstream. In the previous report, we proved this changeable character in vitro, but did not examine in vivo tumor targeting.

Several works on polymeric micelles as MRI contrast agents were reported recently [19–22]. The combination of drug targeting and imaging probes, such as MRI contrast agents, relative to polymer micelles systems has strengthened the effectiveness of chemotherapy [23]. Poly(L-glutamic acid)-*b*-polylactide and polysuccinimicde derivatives were synthesized as a polymeric micelle-based MRI contrast agent [20,21]. Several studies have examined polymeric micelle-based MRI contrast agents, but so far, significant enhancements of MR images at solid tumors through accumulation of the polymeric micelles have not been obtained. One of the challenges that confront the use of MRI contrast agents to detect solid tumors is the selective delivery of the contrast agents to solid tumors by means of the EPR effect. From our experience of anti-cancer drug targeting with polymeric micelle carriers, we assume that an important key for successful tumor targeting is suppression of the incorporated drug's interactions with cells and proteins, in particular, hydrophobic interactions. In our previous report, we showed that polymeric micelles exhibiting lower levels of hydrophobic interactions provided higher levels of antitumor activities, possibly through more efficient passive targeting [24]. If this assumption is applied to MRI contrast agents, the micelle outer shell with a biologically inert character is preferable. Therefore, we have chosen a micelle design with the inert poly(ethylene glycol) outer shell and the contrast species (Gd ion)-containing inner core. Furthermore, we have chosen a negatively charged inner core, not a positively charged one, since positive charges are known to induce strong interactions with the reticuloendothelial system (RES) [25]. Consequently, strong interactions with the RES drastically lower the targeting efficiency relative to solid tumors.

In this report, we synthesized negatively charged block copolymers based on a poly(ethylene glycol)-*b*-poly(L-lysine) system to obtain a long-circulating polymeric micelle MRI contrast agent. This negatively charged block copolymer was found to form a polymeric micelle structure without an addition of positively charged macromolecules. Blood circulation, biodistribution, and excretion of the contrast agents were evaluated. MR images of mice were taken after an injection of the contrast agent, and these images were compared before the injection. According to the findings, polymeric-micelle MRI contrast agent appears to be a strong tool for polymeric-micelle-based drug targeting and for visualizing the location of the carriers at the solid tumor tissues.

2. Materials and methods

2.1. Materials

For the current study, α-methoxy-ω-aminopropyl-poly(ethylene glycol) (PEG-NH_2, $M_w = 5200$) was purchased from NOF Corporation, Tokyo, Japan, and benzene-based lyophilization was carried out before use. A chelating agent active ester, 1,4,7,10-tetraazacyclododecane-1,4,7,10-tetraacetic acid mono (*N*-hydroxysuccinimide ester) (DOTA-OSu), was purchased from Macrocyclics, Texas, USA. Deuterium solvents were purchased from Sigma-Aldrich, Tokyo, Japan. Dehydrated DMF and gadolinium chloride hexahydrate ($GdCl_3 \cdot 6H_2O$) were purchased from Wako Pure Chemicals Industries, Ltd., Tokyo, Japan. We used all these commercial reagents as purchased. The dialysis membrane Spectrapor 6 (molecular weight cut off (MWCO) = 1000) was purchased from Spectrum Laboratories Inc., Tokyo, Japan. ^1H NMR spectra were recorded on a Varian UNITY INOVA 400 MHz NMR spectrometer. To measure gadolinium ion contents in the block copolymer, we used inductively coupled plasma (ICP) with an SPS7800 apparatus (SII NanoTechnology Inc., Tokyo, Japan). Dynamic

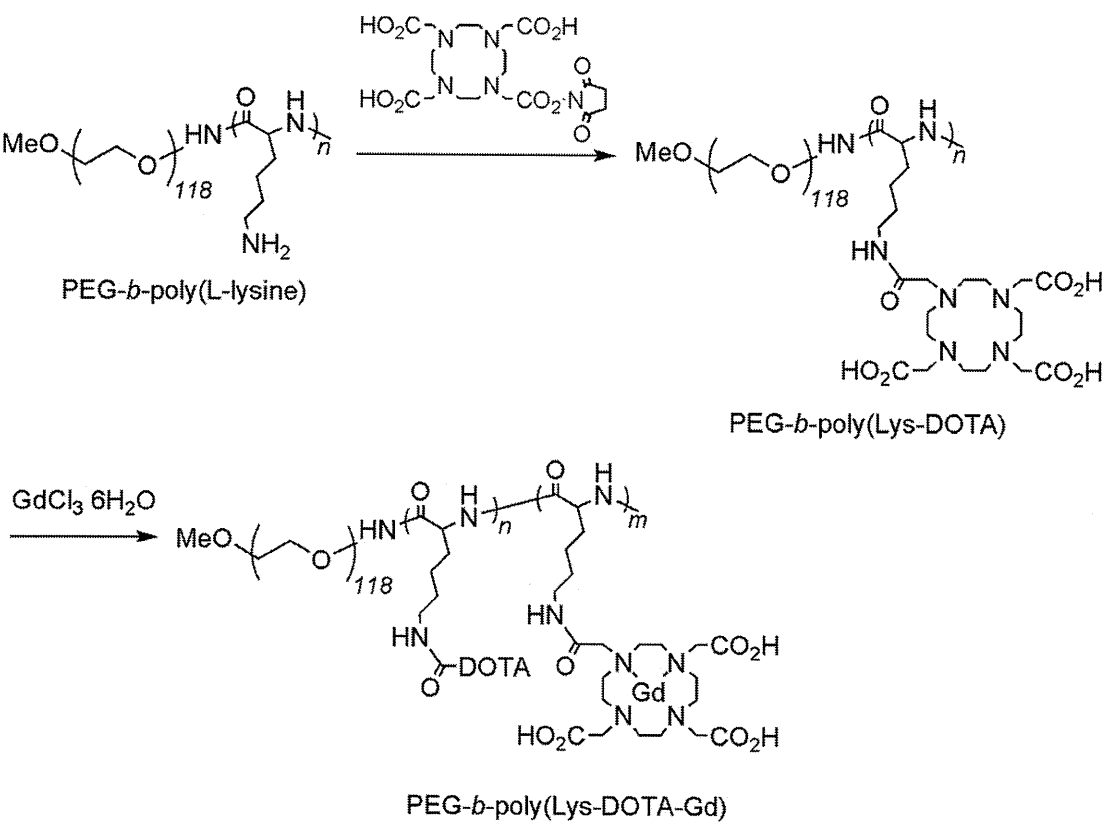

Fig. 1. Synthesis of PEG-P(Lys-DOTA-Gd).

light scattering (DLS) measurements were carried out at 24.5 °C with a DLS-700 instrument (Otsuka Electronics Co., Ltd., Tokyo Japan). Measurement of zeta-potential was performed with an ELSZ-2 instrument (Otsuka Electronics Co., Ltd., Tokyo Japan).

2.2. Animals

Five-week-old ddY female mice and CDF_1 female mice were purchased from the Sankyo Labo Service Corporation, Tokyo, Japan. All animal experiments were carried out in accordance with the guidelines of the Guiding Principles for the Care and Use of laboratory Animals of Hoshi University.

2.3. Synthesis of PEG-P(Lys-DOTA)

A synthesis of a chelate moiety-binding block copolymer is shown in Fig. 1. A poly(ethylene glycol)-*b*-poly(L-lysine) block copolymer (PEG-P(Lys)) was prepared through acid hydrolysis of a poly(ethylene glycol)-*b*-poly[ε-(benzyloxycarbonyl)-L-lysine] (PEG-P(Lys(Z)) block copolymer [26]. We synthesized PEG-P(Lys)s from PEG-NH_2 (molecular weight of PEG-NH_2 = 5200). The compositions of PEG-P(Lys)s were determined by means of ^1H NMR in D_2O under an acidic condition. A mixture of PEG-P(Lys) (86.0 mg), and 1,4,7,10-tetraazacyclododecane-1,4,7,10-tetraacetic acid mono (*N*-hydroxysuccinimide ester) (DOTA-OSu, 308.0 mg) in 8.6 mL of dry DMF was stirred, and then, dry triethylamine (0.5 mL) was added to this reaction mixture. The reaction mixture was stirred overnight at 50 °C. The resulting mixture was dialyzed, at first, against 0.02 N HCl and, then, against distilled H_2O 5 times. The obtained polymer was dissolved in H_2O (at a polymer concentration higher than 15 mg/mL) again, and dialyzed against H_2O 3 times, and we obtained poly(ethylene glycol)-*b*-poly(L-lysine-DOTA) (PEG-P(Lys-DOTA)) by means of lyophilization (162.8 mg). The composition of PEG-P(Lys-DOTA) was determined by means of ^1H NMR in D_2O under an alkali condition (pH > 10). The number of bound DOTA units per polymer chain was calculated from the peak area ratio among CH_2 protons of PEG at 3.73 ppm, 24H protons of DOTA, and 2H protons of lysine in the range of 3.36–2.18 ppm. ^1H NMR (ppm, D_2O + NaOD): 4.08 (s, CH of lysine units), 3.73 (s, CH_2 of PEG), 3.39 (s, OCH_3 of terminal PEG), 3.36–2.18 (m, 24H of DOTA and CH_2 of lysine), and 2.18–1.10 (m, 6H of lysine).

2.4. Gadolinium (III) chelation to PEG-P(Lys-DOTA)

$GdCl_3 \cdot 6H_2O$ (35.0 mg, 0.094 mmol) was added to PEG-P(Lys-DOTA) (153.3 mg) in H_2O (15.0 mL), and the pH of the solution was maintained between 6.0–6.5. The reaction mixture was stirred for 3 h at 50 °C, followed by dialysis against distilled H_2O 5 times. PEG-P(Lys-DOTA-Gd) was obtained as a white solid after lyophilization (160.8 mg). The determination of gadolinium ions in the block copolymer was carried out by means of ICP measurements (7.0 wt.%, the number of gadolinium ions per polymer chain was 6.7). The obtained PEG-P(Lys-DOTA-Gd) is indicated as 118-17-17-7 (PEG unit = 118, lysine units = 17, DOTA moieties = 17, number of gadolinium ion = 7).

2.5. Blood concentration of PEG-P(Lys-DOTA-Gd) micelles in mice

Blood samples (10–75 μL) from the tail vein ($n = 3$) of mice (ddY) (30–33 g) were collected in heparinized capillary glass. Saline (1.5 mL) was added to the blood samples, and the mixture was centrifuged at 4 °C for 4 min at 13,000 rpm. The supernatant of the plasma solution was collected, and the gadolinium ion contents of the block copolymer were measured by means of ICP. The plasma and blood volume were calculated as 0.0488 mL/g body weight for plasma and 0.0778 mL/g body weight for blood, respectively.

2.6. Biodistribution of the contrast agents

Biodistribution of the contrast agents was evaluated in CDF_1 female mice (5 weeks old) (20–22 g) bearing a colon 26 tumor. Colon 26 cells (1.0×10^4 cells/0.1 mL) were transplanted into CDF_1 female mice subcutaneously. Injection of the contrast agents was started 9–10 days after the transplantation. Tumor volumes were approximately 50–100 mm^3. The tumor volumes were calculated as follows: volume = $1/2LW^2$; L is the long diameter and W is the short diameter of a tumor.

Twenty-four hours after the injection, the blood was collected with a heparinized syringe and centrifuged at 4 °C for 4 min at 13,000 rpm. The plasma was obtained, and its gadolinium content was measured by means of ICP. The major tissues including tumor tissues were excised and weighted. For the determination of gadolinium ion content in the tissue, saline was added to the tissues, followed by an addition of nitric acid (conc. 70%) and sulfuric acid (conc. 98%). Then, the mixture was heated. A saturated aqueous oxoammonium solution was added to the yellow mixture and heated again. The resulting pale-yellow mixture was diluted with saline. The supernatant was collected, and its gadolinium content was measured by means of ICP. The urine ($n = 3$) was collected 24 h and 48 h after injection, and its gadolinium content was measured by means of ICP.

2.7. MR imaging of mice tumor model

MR imaging was performed with female mice (CDF_1) bearing a colon 26 tumor. The tumor transplantation was carried out as described in 2.6. The contrast agents were injected at a dose of 0.05 mmol of Gd/kg into a mice-tail vein. MR images were taken with a Varian NMR system at 9.4 T. T_2-weighted fast spin echo (TR = 2500 ms, ETL = 8, ESP = 4, effective TE = 48) was performed for all experiments before following the T_1-weighted gradient echo protocol. T_1-weighted gradient echo protocol was followed before the injection, immediately after the injection, and then 4 h and 24 h after the injection. Imaging parameters of the T_1-weighted images were TR/TE = 8.0/4.2, flip angle = 30°, field of view of 50 × 30 mm, a matrix size of 192 × 192, and 2 mm of coronal slice thickness, and were TR/TE = 8.0/4.5, flip angle = 30°, field of view of 45 × 45 mm, a matrix size of 192 × 192, and 2 mm of axial slice thickness. For normalized signal intensity relative to the T_1-weighted images, the tumor area was selected as a region of interest (ROI). The signal intensity of the ROI was compared with the intensity of a stock solution of 0.1 mM gadolinium ion in agarose gel. The relative signal intensity of the ROI

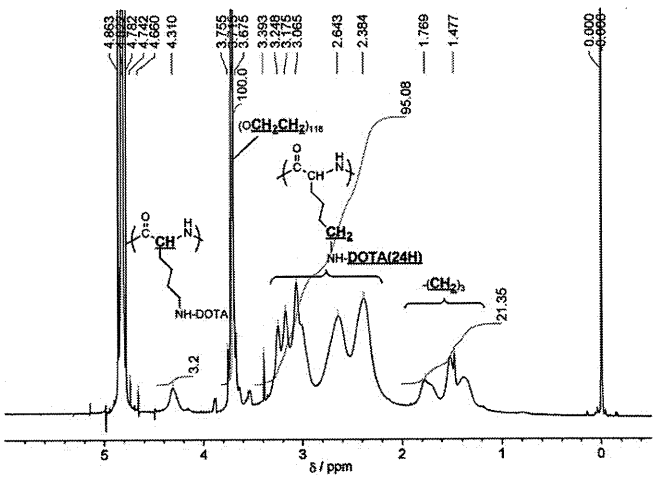

Fig. 2. ^1H NMR spectrum of PEG-P(Lys-DOTA) (118-17-17) in D_2O + NaOD.

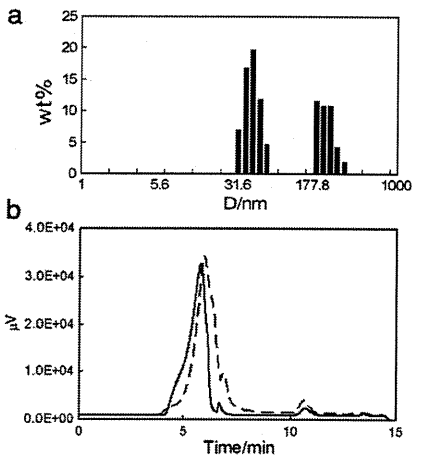

Fig. 3. (a) Weight–weight average size distribution of PEG-P(Lys-DOTA-Gd) micelle (118-17-17-7) in 150 mM NaCl measured by DLS, and (b) gel-permeation chromatogram of PEG-P(Lys-DOTA-Gd) micelle in H_2O (1.2 mg/mL) of concentrated preparation of 118-17-17-7(solid line) and diluted preparation of 118-17-17-6 (dashed line).

24 h after the injection was compared with the signal intensity before the injection.

3. Results and discussion

3.1. Block copolymer synthesis and characterization of polymeric micelle

A block copolymer binding DOTA groups was synthesized from poly(ethylene glycol)-*b*-poly(L-lysine). The binding of a DOTA at the lysine residues was carried out with a coupling reaction between a primary amine and an NHS ester of a DOTA reagent, as shown in Fig. 1. Poly(ethylene glycol)-*b*-poly(L-lysine-DOTA) block copolymers possessing 5200 of molecular weights, and 17–21 units of the DOTA-bound lysine moiety were obtained. Quantitative substitution of lysine residues for DOTA was confirmed in ^1H NMR spectra as shown in Fig. 2.

A fully DOTA-substituted block copolymer formed polymeric micelles after the dialysis in dist. H_2O at a polymer concentration of 15 mg/mL. The quantitative DOTA conjugation was essential for the polymeric micelle formation. Insufficient DOTA conjugation, such as 118-22-19 wherein the number of DOTA residues was 19 out of 22 lysine residues, did not form a polymeric micelle. This result shows that the micelle structures were not formed in the presence of a small amount of unmodified lysine residue (3 out of 22 residues); the result also underscores the importance of strong interactions among the conjugation DOTA units for the micelle formation.

Gadolinium ion was partially chelated to DOTA in the block copolymer, poly(ethylene glycol)-*b*-poly(L-lysine-DOTA). Gadolinium-chelated poly(ethylene glycol)-*b*-poly(L-lysine-DOTA-Gd) maintained the polymeric micelle formation. Dynamic light scattering (DLS) and GPC measurements of the gadolinium chelated block copolymers, 118-17-17-7 which is 118 ethylene glycol units, 17 lysine residues, 17 DOTA conjugation to lysine residues, and 7 gadolinium ions at DOTA were performed. Fig. 3(a) shows a DLS chart of this block copolymer micelle with a weight average of 42.9 ± 7.6 nm (mean $\pm$ SD), accompanied by a secondary aggregation of a weight average of 225.5 ± 53.0 nm (mean $\pm$ SD). Similar secondary aggregation was also found in the precursor of PEG-*b*-poly(L-lysine-DOTA-Gd) (data in supplemental section).

The zeta-potential of the obtained polymeric micelle showed -9.55 mV in 150 mM NaCl solution, indicating that the polymeric micelle was negatively charged. This negative value was given from a vacant DOTA moiety having 3 carboxylic acids and 4 tertiary amines. The tertiary amines of DOTA could work as only two cationic species in the physiological condition owing to their excessively close proximity to each other, whereas three carboxylic acids in the DOTA moiety could work as 3 anions owing to their long distances from one other. As a result, the total charge of the polymeric micelles exhibited negatively charged particles. In general, cationic species are more quickly scavenged by the reticloendothelial system than anionic species [25]. This scavenging is a big obstacle for the passive tumor targeting through the EPR effect. For the design of a tumor-targeting system, a slightly negative-charged particle is preferable as an inert carrier.

GPC measurements of the polymeric micelle (1.2 mg/mL in H_2O) were performed by the use of an HPLC system (LC 2000 series, Jasco, Tokyo, Japan) equipped with a TSK-gel G4000-PW_{XL} column (eluent = H_2O, flow rate = 1.0 mg/mL, detector = RI) at 40 °C. Even in such a diluted aqueous solution of the block copolymer, both DLS and GPC measurements clearly exhibit the formation of the polymeric micelle as shown in Fig. 3(b) (solid line). This finding indicated that once the polymeric micelle was formed by interactions among vacant DOTAs, the polymeric micelle was not dissociated in a time scale of a DLS and GPC measurement under dilution. When we injected a similar sample 118-17-17-6 prepared from a dilute condition (3 mg/mL), the peak of the polymeric micelle was shifted to a longer elution time as shown in Fig. 3(b) (dashed line). This result indicates a considerable polymer concentration effect on the formation of the polymeric micelle; namely, strong interactions among vacant DOTA moieties at a high concentration.

Formation of the polymeric micelle with or without a gadolinium ion appears to depend on interactions among vacant DOTAs as described above. To prove this interaction, we added an excess of $GdCl_3$ (2.0 mol equivalent vs DOTA) into 118-20-20 to prepare complete chelation of the DOTA units with gadolinium ions. However, we found that the composition of the block copolymer was 118-20-20-16. Even when we added the excess amount of gadolinium ions to the block copolymer, we obtained 20% of vacant DOTA in the block copolymer. This result implies that DOTA–DOTA interactions prevent gadolinium ion from freely chelating into a DOTA moiety. When we injected this block copolymer into the GPC column, we observed that the peak of around 5–6 min. corresponded to the polymeric micelle disappeared. This disappearance indicates that chelation of a high level of gadolinium ion in a block copolymer resulted in so unstable micelle formation on the GPC column. We concluded that the polymeric micelle was formed through the interactions among vacant DOTAs, and that these interactions depend on the block copolymer concentrations and on the numbers of the chelated gadolinium ions.

3.2. Blood circulation of the polymeric micelle MRI contrast agent

The polymeric micelle, 118-17-17-7, was injected at a dose of 0.05 mmol Gd/kg, into a mouse-tail vein for pharmacokinetic

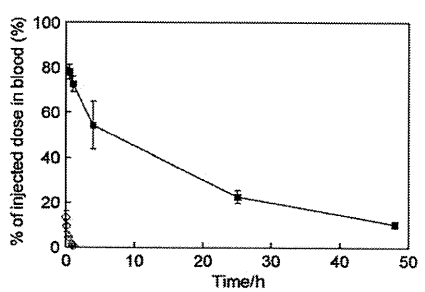

Fig. 4. Blood-concentration time course of PEG-P(Lys-DOTA-Gd) micelle (118-17-17-7) in ddY female mice at a dose of 0.05 mmol Gd/kg (■), and Gd-DTPA at a dose of 0.10 mmol Gd/kg (◇). After defined time periods (0.5 h, 1 h, 2 h, 4 h, 24 h, and 48 h), the blood samples were collected into capillary glass tubes via mice's tail veins.

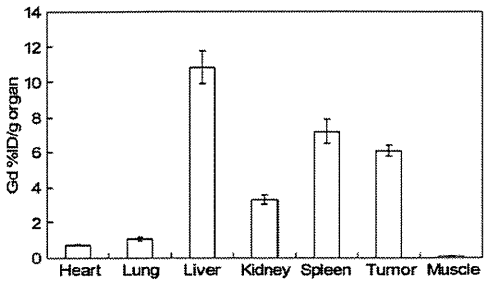

Fig. 5. Biodistribution of PEG-P(Lys-DOTA-Gd) micelle 24 h after injection at a dose of 0.05 mmol Gd/kg.

observations. The blood concentrations of the polymeric micelles were measured by means of ICP. Fig. 4 shows the blood concentration-time course of the polymeric micelles until 48 h after the injection. A low-molecular-weight gadolinium ion complex, such as Gd–DTPA, was immediately excreted 1 h after injection (only 1.4 ± 0.8% was found in blood). On the other hand, the polymeric micelle remained 22.5 ± 2.9% and 10.2 ± 1.4% (mean ± SD) in blood at 24 h and 48 h after the injection, respectively. These high blood concentrations exhibit significantly stable circulation of the polymeric micelle in blood. This polymeric micelle underwent an approximately 10-fold dilution relative to the injection in blood: however, stable formation of the polymeric micelle at such diluted conditions was confirmed in this in vivo experiment. This stable blood-circulation time-course was similar to the system of anti-cancer drug-incorporating polymeric micelle, a doxorubicin-incorporating poly(ethylene glycol)-*b*-poly (aspartic acid) system [1]. According to reports, the doxorubicin-incorporating polymeric micelle system provides a drug concentration of 24.6% of the injected dose (ID) after 24 h in the blood. Such a long circulating property of the doxorubicin-incorporating polymeric micelle successfully led to highly selective tumor accumulation. Owing to this similar pharmacokinetic behavior, this MRI contrast agent can be a strong tool for estimation of the pharmacokinetic behavior of "anti-cancer drug"-incorporating polymeric micelles.

3.3. Biodistribution and excretion of the polymeric micelle MRI contrast agent

Selective and high accumulation of drug carriers at solid tumors is essential for an improvement of anticancer drug efficacy. As well as the drug-targeting systems, selective and high accumulation is desired for diagnostic agents.

In recent decades, polymeric micelles have constituted one of the best drug-carriers to have achieved selective accumulation of an anti-cancer drug, through the EPR effect, at solid tumor tissues [1]. Biodistribution of the polymeric micelle contrast agents was evaluated in CDF_1 female mice bearing the colon 26 tumor. Fig. 5 shows the percentage of the injected dose of the polymeric micelle 24 h after the injection in the normal organs as well as in tumor tissues. The study showed that the accumulation of the polymeric micelle contrast agent in tumor tissues reached 6.1 ± 0.3% ID (injected dose)/g of tumor. This accumulation amount was considerably high. Furthermore, highly selective delivery was present with low accumulation amounts in heart, kidney, and muscle tissue. For the mononuclear phagocyte system (MPS), this contrast agent was found to be accumulated in 10.8 ± 0.9 and 7.2 ± 0.7% ID/g of liver and spleen, respectively. These accumulation ratios were similar to those in case of doxorubicin-incorporated polymeric micelle, but better tumor/muscle ratios were obtained in this MRI contrast agent [1]. This difference may rest on a difference in micelle size as well as in detection species: there is a physically entrapped drug for the drug-carrying micelles and there are chelated gadolinium ions for the MRI contrast agent. The gadolinium-binding macromolecular

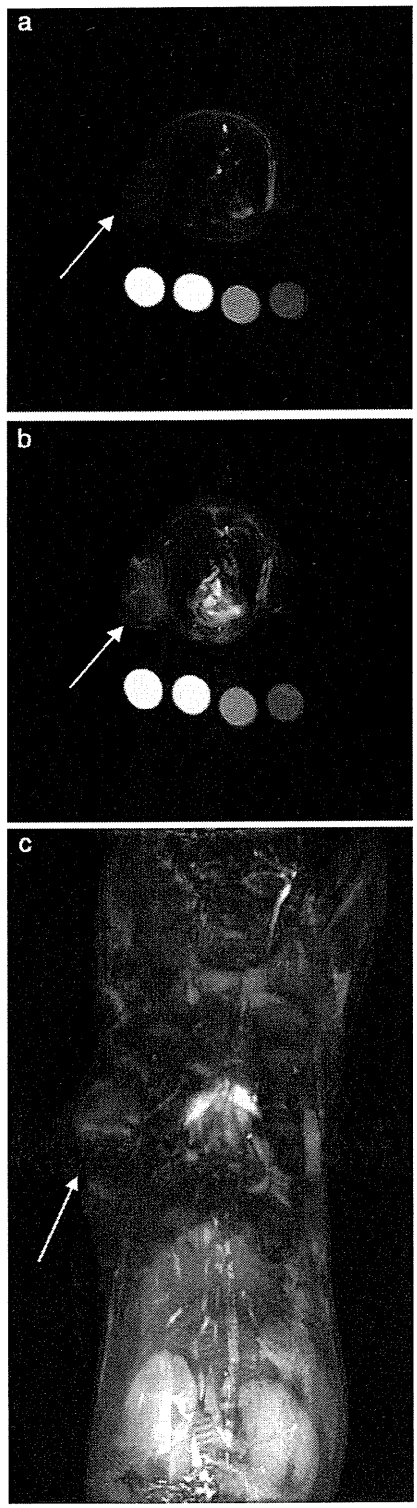

Fig. 6. Axial slices of MR images (a) before and (b) 24 h after the injection at a dose of 0.05 mmol Gd/kg. Tumor areas are on the left side in the axial slices. The circles indicate the stock solutions of (left to right) 1.0 mM, 0.5 mM, 0.1 mM gadolinium ion in agarose gel and blank in agarose gel. T_1-weighted gradient echo protocol was used. Parameters of the T_1-weighted images were TR/TE = 8.0/4.5, flip angle = 30°, field of view of 45 × 45 mm, a matrix size of 192 × 192, and 2 mm of axial slice thickness. Arrows indicate tumor tissue. (c) MIP images of coronal slices 24 h after injection. Arrow indicates tumor. Parameters of the T_1-weighted images were TR/TE = 8.0/4.2, flip angle = 30°, field of view of 50 × 30 mm, a matrix size of 192 × 192. MIP images were obtained by 2 mm thickness × 4 slices.

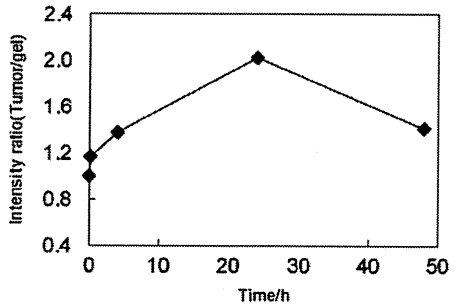

Fig. 7. Relative signal intensities of tumor area at defined time (0 h, 4 h, 24 h, 48 h) after the injection of the polymeric micelle MRI contrast agent.

carrier may not penetrate into muscle as do low-"molecular weight" drugs that are released from the carrier.

Wang Y et al. reported that poly[N-(2-hydroxypropyl)methacrylamide] (PHPMA) [14] gadolinium-conjugates exhibited size-dependent tumor accumulation. They stated that a large molecular weight of PHPMA (121 kDa) gadolinium conjugate exhibited the best tumor accumulation at 7 days after injection. Although, Bogdanov A et al. reported another example of successful passive targeting to solid tumors with a graft copolymer of poly(ethylene glycol) featuring poly(L-lysine) [9]. This contrast agent exhibited tumor targeting with a long blood-circulation time ($t_{1/2}=36$ h): however, this long-circulation property in blood indicates that the contrast agent cannot excrete smoothly from the body owing to the polymer's very large molecular weight (690 kDa). The researchers synthesized different molecular weights of similar polymers to compare the polymers' biodistribution [10] and found that the polymers accumulated at solid tumors in a "molecular-weight"-dependent manner. This molecular-weight dependency indicated that smaller molecular weights of polymers can be excreted through the kidneys.

These above-mentioned polymers exhibited better tumor accumulation, corresponded to larger molecular weights of the polymers. However, the excretion of the contrast agent, especially in the case of the macromolecular contrast agent, is a serious matter for the development of diagnostic agents.

Therefore, we checked the kidneys' excretion of our polymeric micelle contrast agent. In urine, $20.8\pm7.6\%$ of the polymeric micelle was found 48 h after the injection. This result indicates that the polymeric micelle was excreted through the kidney filtration. Since the size of the polymeric micelle contrast agent was 50–250 nm as shown in Fig. 3(a), the polymeric micelles cannot pass through the kidney filtration. Therefore, these polymers that formed in urine appears to have passed through the kidney filtration in a dissociated polymer form, since the average molecular weight of this block copolymer is only 15,000. This is an excellent property of the polymeric micelle MRI contrast agent; namely, this agent exhibits long circulation in blood in a micelle form, while this agent can be excreted through the kidneys in a dissociated polymer form.

Furthermore, the obtained polymeric micelle MRI contrast agent delivered a larger amount to solid tumors than did previously reported macromolecular MRI contrast agents that can be also excreted from the kidneys (agents such as PHPMA gadolinium-conjugate [14] and graft copolymer of poly(ethylene glycol) with poly (L-lysine) [10]).

In order to estimate possible acute toxicity, we injected the 4-fold of the volume of the contrast agent into the mouse tail vein, and observed the body weight change over the course of 16 days. There was no significant difference in comparison to the control (less than $\pm10\%$). Although we have to conduct further experiments to obtain toxicity-related information of greater exactness, these preliminary results indicate that this polymeric micelle can dissociate and be excreted from the kidneys, and that this tumor targeting results a passive targeting mechanism (the EPR effect). In a future study, we would like to optimize the pharmacokinetics and the dissociation behavior of the polymeric micelles by controlling the composition of the block copolymers.

3.4. MR imaging at tumor tissue

We took an MR image of the tumor-bearing mouse after the injection of the polymeric micelle contrast agent. Fig. 6 shows T_1-weighted MR images of tumor tissues before and after 24 h at an injection dose of 0.05 mmol Gd/kg. After the injection of the polymeric micelle, MR images exhibited a significant signal enhancement at the kidneys. This signal enhancement at the kidneys indicates that kidneys excreted the contrast agent, as shown in Fig. 6(c). However, even 24 h after the injection, an intense signal was observed in the heart and aorta areas. This indicates that a considerable amount of the contrast agent was circulating in the bloodstream, as described in pharmacokinetic results. The relative signal intensity at axial slices of the tumor tissues underwent a 2.0-fold increase after 24 h, as compared with the signal before the injection. The signal intensity of the tumor area had gradually increased by 24 h and had slightly decreased by 48 h, as shown in Fig. 7. This behavior of the signal intensities is similar to the doxorubicin concentration delivered by the polymeric micelle carrier system. All these results indicate that the enhancement of MR signals in the tumor area rested on the successful passive accumulation of the MRI contrast agent at solid tumors.

4. Conclusion

We prepared polymeric micelle MRI contrast agents using poly (ethylene glycol)-*b*-poly(L-lysine) block copolymers. A reaction of poly(ethylene glycol)-*b*-poly(L-lysine) with a DOTA derivative resulted in a quantitative DOTA conjugation regarding the lysine residues of the block copolymer, and the obtained block copolymer formed a polymeric micelle. This micellar structure was maintained after a partial chelation of the DOTA moiety with gadolinium ions. The biodistribution and the excretion of the polymeric micelle was evaluated in colon 26-bearing CDF_1 female mice. Selective accumulation of the polymeric micelle at the tumor tissues was observed 24 h after the injection. The contrast agent's accumulation substantially enhanced the signal intensity of the MR images at the tumor. This polymeric micelle MRI contrast agent will be a useful diagnostic tool, particularly in combination with a polymeric micelle-based drug-targeting system.

Acknowledgement

This work was supported by the Ministry of Health, Labour, and Welfare of Japan. K. Shiraishi and M. Yokoyama acknowledge the support from the Program for Promoting the Establishment of Strategic Research Centers, Special Coordination Funds for Promoting Science and Technology, the Ministry of Education, Culture, Sports, Science and Technology of Japan, and Tokyo Ohka Foundation for the Promotion of Science and Technology.

Appendix A. Supplementary data

Supplementary data associated with this article can be found, in the online version, at doi:10.1016/j.jconrel.2009.01.010.

References

[1] M. Yokoyama, T. Okano, Y. Sakurai, S. Fukushima, K. Okamoto, K. Kataoka, Selective delivery of adriamycin to a solid tumor using a polymeric micelle carrier system, J. Drug Target. 7 (3) (1999) 171–186.